AN ENHANCED TRANSIENT SOLID OXIDE FUEL CELL PERFORMANCE MODEL

A Thesis
Presented to
The Academic Faculty

By

James Christopher Ford

In Partial Fulfillment
Of the Requirements for the Degree
Master of Science in Mechanical Engineering

Georgia Institute of Technology

December 2006

AN ENHANCED TRANSIENT SOLID OXIDE FUEL CELL PERFORMANCE MODEL

Approved by:

Dr. Comas Haynes, Research Co-Advisor
Georgia Tech Research Institute
Georgia Institute of Technology

Dr. Samuel Graham, Academic Co-Advisor
School of Mechanical Engineering
Georgia Institute of Technology

Dr. Sam Shelton
School of Mechanical Engineering and
Department of Academic Affairs
Georgia Institute of Technology

Dr. Peter Hesketh
School of Mechanical Engineering
Georgia Institute of Technology

Date Approved: November 10, 2006

ACKNOWLEDGEMENTS

I would first like to thank the good Lord for supplying His grace to finish this work. The Lord has provided people of excellence to help complete the present thesis. First, I would like to thank my lead research advisor, Dr. Comas Haynes, for loving me as his "academic son." Without Dr. Haynes' love, guidance, and support, this work could not have been completed, nor would I have grown into a man in pursuit of excellence. I would also like to thank my academic co-advisor, Dr. Sam Graham, Dr. Peter Hesketh, and Dr. Sam Shelton who as members of my reading committee offered larger scope perspectives and valuable insights which further enhanced this work.

Furthermore, I would like to express love and thanks to my wonderful family. My always supportive parents, Robert and Catherine Ford, whom have instilled the value of education which enabled me to complete this work. And my three siblings, Angela, Robert, and Knatokie whom always provide timely words of encouragement. I love you all so very much.

TABLE OF CONTENTS

ACKNOWLEDGEMENTS iii

LIST OF TABLES vi

LIST OF FIGURES vii

NOMENCLATURE xii

SUMMARY xv

CHAPTER 1: INTRODUCTION 1

CHAPTER 2: LITERATURE REVIEW 6

CHAPTER 3: ELECTRICAL TRANSIENTS WITHIN SOFCS 14

- 3.1 SOFC operation 14
    - 3.1.1 Chemistry and Electrochemistry Associated with the SOFC 14
- 3.2 Electrical Transients Model 23
    - 3.2.1 Motivation 23
    - 3.2.3 Model Algorithm 24
    - 3.2.4 Sample Electrical Transient Results and Discussion 31

CHAPTER 4: COMPLEMENTARY MODELING 35

- 4.1 Time Scale of Dynamic Modeling of SOFCs 35
- 4.2 Time Constants Analysis 36
    - 4.2.1 Methodology 36
    - 4.2.2 Time Constant Analysis Results and Discussion 39
    - 4.2.3 Time Constant Analysis as FRT→ ∞ 49
    - 4.2.4 Conclusions of Time Constants Analysis 51
- 4.3 Electrolysis Modeling 51

    4.3.1 Motivation and Problem Description 51
    4.3.2 Electrolysis Simulation Methodology 52
    4.3.3 Sample Results and Discussion of Electrolysis Modeling 53
    4.3.4 Conclusions of the Electrolysis Simulations 57

CHAPTER 5: ELECTROCHEMICAL LIGHT OFF SIMULATION 58

  5.1 Problem Description 58
  5.2 Model Description 59
  5.3 Sample Results and Discussion 61
  5.4 Conclusions of Electrochemical Light Off 68

CHAPTER 6: CONCLUSIONS 69

  6.1. Summary 69
  6.2 Conclusions of Electrical Transient Modeling 69
  6.3 Complementary Modeling Conclusions 70
    6.3.1 Time Constant Analysis 70
    6.3.2 Electrolysis Modeling 71
  6.4 Conclusions Electrochemical Light Off Simulations 72

REFERENCES 75

APPENDIX 80

LIST OF TABLES

Table 3.1. Chemical Reactions for methane reformation SOFC. 15

Table 3.2. Electrochemical reactions for SOFC operation. 15

Table 3.3. Initial and final steady-state conditions for a transient simulation. 29

Table 4.1. Initial conditions for the time constant simulations. 39

Table 4.2. Time constant results for the first case. 40

Table 4.3. Second case initial conditions. 41

Table 4.4. Time constant results for the second case. 41

Table 4.5. Hydrogen partial pressure values to illustrate the reason for time constant dependence on initial current demand for a 30% increase in load. 42

Table 5.1. Three electrochemical scenarios considered for the electrochemical light off simulations. 61

Table 5.2. SOFC unit cell data and property values. 62

Table 5.3. Final steady state cell efficiencies. 65

LIST OF FIGURES

Figure 1.1. Solid oxide fuel cell fundamentals (courtesy of www.eere.energy.gov). 2

Figure 1.2. Cross-sectional view of a SOFC unit cell (not to scale). 3

Figure 1.3. Fuel cell system inclusive of stack (“power section”) and b-o-p. 3

Figure 2.1. Discretization methodology that facilitated the 1-D performance model of a TSOFC by Haynes and Wepfer [12]. 8

Figure 2.2. Equivalent circuit method to solve for voltage and current distributions within a PSOFC [11]. 9

Figure 2.3. Equivalent circuit method for a TSOFC to solve for voltage and current distributions [7]. 9

Figure 2.4. Lagrangian approach showing the connection between spatial and temporal discretization [4]. 10

Figure 3.1. Control volume for the analysis of a solid oxide fuel cell. (Note that lengths of the arrow do not indicate relative amount or value.) 15

Figure 3.2. Polarization curve showing the various loss mechanisms (i.e. polarizations) that occur during fuel cell operation [23]. 18

Figure 3.3. Diagram of the mechanism of concentration polarization stemming from a limiting current [14]. 21

Figure 3.4. Illustration of the discretization of the cell which is a key aspect of the electrical transients modeling approach [4]. 25

Figure 3.5. Electrical transients model flowchart ("Intra-packet" level). 28

Figure 3.6. Electrical transients model algorithm ("Inter-packet" level). 29

Figure 3.7. Illustration of the rediscretization solution of the mole fraction distribution problem that arises when the number of slices changes due to a change in fuel flow rate. 31

Figure 3.8. Electrical transient responses to bi-modal stimuli of a current density step change of 350 to 600 mA/cm^2 with fuel ramp rate times (FRT) of zero, one, and three seconds. (Note how increasing FRT results in a more pronounced overshoot and undershoot in the fuel utilization and voltage profiles, respectively.) 32

Figure 4.1. Diagram showing the three distinct dynamic time scales associated with SOFCs: thermal transients (on the order tens of minutes), electrical transients (on the order of seconds), and anodic mass transfer transients (on the order of fractions of seconds). 35

Figure 4.2. Hydrogen mass diffusion through the porous anode. 36

Figure 4.3. The lumped capacitance approach for developing a bulk average partial of hydrogen in the porous electrode. 38

Figure 4.4. Time constant ratio (electrical: mass transfer) mapping showing dependence on initial current demand and percent load increase. 43

Figure 4.5. Anodic mass transfer time constant mapping showing dependence on initial current demand and percent load increase. 43

Figure 4.6. Electrical time constant mapping showing dependence on initial current demand and percent load increase. 44

Figure 4.7. Time constant ratio (electrical: mass transfer) mapping showing dependence on initial current demand and percent load increase with ASR changed to 0.50 Ω-cm^2. 45

Figure 4.8. Anodic mass transfer time constant mapping showing dependence on initial current demand and percent load increase with ASR changed to 0.50 Ω-cm^2. 45

Figure 4.9. Electrical time constant mapping showing dependence on initial current demand and percent load increase with ASR changed to 0.50 Ω-cm^2. 46

Figure 4.10. Time constant ratio (electrical: mass transfer) mapping showing dependence on initial current demand and percent load increase when anode thickness is decreased to 0.04 cm. 47

Figure 4.11. Electrical time constant mapping showing dependence on initial current demand and percent load increase when the anode thickness is decreased to 0.04 cm. 48

Figure 4.12. Anodic mass transfer time constant mapping showing dependence on initial current demand and percent load increase when the anode thickness is decreased. 48

Figure 4.13. Time constant ratio (electrical: mass transfer) mapping showing dependence on initial current demand and percent load increase. 49

Figure 4.14. Time constant ratio (electrical: mass transfer) mapping showing dependence on initial current demand and percent load increase. 50

Figure 4.15. Diagram illustrating downstream electrolysis due to planned or unplanned steep decreases in load. 52

Figure 4.16. Zero current position profile as a function of initial fuel utilization and decrease in current demand. 53

Figure 4.17. 2-D projection of electrolysis occurrence (shaded region) as a function of decrease in current demand and initial fuel utilization. Note that at higher fuel utilizations smaller decreases in current demand are sufficient to cause electrolysis. 54

Figure 4.18. Zero current position profile as a function of fuel utilization and the resulting voltage gain. 55

Figure 4.19. A projection of voltage gain vs. initial fuel utilization from the zero current position profile. 55

Figure 4.20. Graphic showing the impact of fuel utilization (i.e. in the range of 50-85%) on the partial pressure of hydrogen profile. 56

Figure 4.21. Graphic showing the impact of fuel utilization (i.e. in the range of 50-85%) on the Nernst potential profile. (Note how the Nernst potential profile decreases more significantly with increasing fuel utilization.) 57

Figure 5.1. Graphic illustrating the electrochemical light off phenomenon. [Courtesy of Pacific Northwest Laboratory.] 58

Figure 5.2. Flowchart/logic of computational approach of the electrochemical light off simulation. 61

Figure 5.3. SOFC temperature response during electrochemical light off. (Note t*=t/T where T is 83.5 minutes.) 63

Figure 5.4. Heat generated by the cell and the percent of the heat retained by the cell for each scenario of the electrochemical light off simulations. 64

Figure 5.5. Power production for each electrochemical light off simulation. 65

Figure 5.6. Temperature profiles for the galvanostatic and potentiostatic simulations of electrochemical light off. 66

Figure 5.7. Heat generation profiles for the galvanostatic and potentiostatic simulations of electrochemical light off. 67

Figure 6.1. Graphic showing the thermal hysteresis effect caused by electrical load cycling between 300 mA/cm^2 to 500 mA/cm^2 which is impacted by the current density ramp rate (Note CDRR or dj/dt has the units of mA/cm^2/min.) 74

Figure 6.2. Graphic showing the voltage hysteresis effect caused by thermal hysteresis effect. (Note CDRR or dj/dt has the units of mA/cm^2/min.) 74

NOMENCLATURE

ASR	Area Specific Resistance, Ω-cm^2
C_{cell}	Unit Cell Heat Capacitance, J/K
$C_{j,o}$	Concentration of a Reactant in the Free Stream
CDRR	Current Density Ramp Rate, mA/cm^2/min
$D_{a,eff}$	Anode Effective Binary Diffusion Coefficients ,cm^2/s
$D_{c,eff}$	Cathode Effective binary Diffusion Coefficients, cm^2/s
dj/dt	Current Density Ramp Rate, mA/cm^2/min
E	Nernst Potential, V
E°	Standard Pressure Nernst Potential, V
F	Faraday's Constant, 96485 C
FRT	Fuel Ramp Time, s
n_i, n_j	Moles of Constituent i or j, mol
G_i, G_j, G_k	Gibbs Free Energy of Constituent i, j, or k, J
G_k°	Standard Pressure Gibbs Free Energy of Constituent k, J
i''	Current Density, mA/cm^2 or A/m^2
i	Current, mA or A
i_a	Anode Limiting Current Density, mA/cm^2 or A/m^2
i_c	Cathode Limiting Current Density, mA/cm^2 or A/m^2
i_j	Slice Current, mA or A
$i_{l,j}$	Limiting Current Density, mA/cm^2 or A/m^2
i_o	Exchange Current Density, mA/cm^2 or A/m^2
K	Equilibrium Constant

l_a	Anode Thickness, cm
l_c	Cathode Thickness, cm
n	Number of Electrons Transferred per Mole of Fuel, mol
$\dot{n}_j$, $\dot{n}_k$, $\dot{n}_k$	Consumption/Production Rate of a Specie i, j, or k, mol/s
p	Operating Pressure, atm
$p_i, p_j, or\ p_k$	Constituent i, j, or k Partial Pressure Normalized Standard Pressure
P_{avg,int,H_2}	Initial Bulk Average Partial Pressure of Hydrogen, N/cm^2
$\dot{P}_{avg,\text{int},H_2}$	Time Rate of Change of Bulk Partial Pressure of Hydrogen, N/s-cm^2
$P_{avg,slice,H_2}$	Bulk Average Partial Pressure of a Hydrogen in the Anode, N/cm^2
$P_{\text{fuel stream,slice,}\mathrm{H_2}}$	Fuel Stream Partial Pressure of Hydrogen of a Slice, N/cm^2
Q_{gen}	Unit Cell Heat Generated, W
Q_{conv}	Unit Cell Convective Heat Transfer from the Cell to the Reactant Streams, W
$\mathrm{R_i}$	Area Specific Resistance, Ω-cm^2
$\mathrm{R_{mass,transfer}}$	Mass Transfer Resistance, C-m^2/A or C-cm^2/A
R_u	Universal Gas Constant, kJ/mol-K
t	Time, ms, s, or min
T	Temperature, K
T_{cell}	Unit Cell Temperature, K
ν_i	Stoichiometric Coefficients of the Constituents
V	Cell Potential or Voltage, V
V_{ohmic}	Ohmic loss, V
V_{act}	Activation Polarization, V

V_{conc}	Concentration Polarization, V
$W_{\max}$	Maximum Useful Work, J
$\vec{x}$	Fluid Element Position, cm

Recurring Subscripts

avg	Average
CH_4	Methane
CO	Carbon Monoxide
CO_2	Carbon Dioxide
H_2	Hydrogen
H_2O	Steam
intermed	Intermediate
init	Initial
O^{-2}	Oxygen Anions
O_2	Oxygen
Slice	One Computational Segment or Control Volume
Shift	Referring to the Water Gas Shift Reaction

Greek Symbols

α	Charge Transfer Coefficient
Δ	Change
ε	Anode Porosity
η	Lagrangian Fluid element
τ	Time Constant Associated with Electrical or Mass Transfer Transients, s
$\vec{v}$	Fuel Stream Velocity, cm/s

SUMMARY

In order to facilitate the application of solid oxide fuel cells, in conjunction with reduced research and development costs, there is a need for accurate performance models to aid scientists and engineers in component and process design. To this end, an enhanced transient performance model has been developed. The present thesis enhances transient modeling and simulation via characterization of two important transient phenomena. They are bimodal stimuli (i.e., simultaneous changes in reactant supply and load demand) electrical transients, inclusive of the simulation of electrolysis, and the electrochemical light off phenomenon. One key result of the electrochemical light off simulations was that the realization that electrochemical parameters such as cell potential may be used as dynamic control variables during transitional heating of the cell. Reflective of the state-of-the-art in controls and dynamic simulation development, the modeling efforts are completed in the MATLAB computing environment. There is then a tangible software development that accompanies the modeling and simulation exercises and transient insights resolved.

CHAPTER 1

INTRODUCTION

Global energy consumption is rising considerably, and is likely to continue accelerating; however, the forecasted production of energy resources, especially petroleum, is not keeping pace with consumption [1]. This sobering trend justifies an urgency with respect to the need for more efficient, as well as alternative, energy conversion devices. The fuel cell is a leading candidate for alternative power due to its high efficiency and generally environmentally amiable attributes. Fuel cells are similar to batteries in that electricity is produced via electrochemistry, but fuel cells are open systems such that their reactants are externally stored. One particular fuel cell that has shown great potential for large-scale applications is the solid oxide fuel cell (SOFC). SOFCs are high temperature (600^oC -1000^oC) power sources that are considered viable alternatives for residential grid power, backup generators, and other multi-scale (5kW-1MW) power production applications. Among their benefits, they are tolerant to impure hydrogen fuel streams (i.e., they can accommodate, including utilize, carbon monoxide and certain amounts of lower hydrocarbons), and they don't require precious metal catalysts as required for other types of fuel cells such as the Proton Exchange Membrane (PEM) technology.

Unlike PEM cells, SOFC electrolytes are conventionally anionic conductors wherein oxygen anions transport through the electrolyte. In SOFCs, oxygen from air is reduced at the cathode, and hydrogen is oxidized at the anode. Usable heat, water vapor, and possibly carbon-dioxide are the products of the electrochemical reaction. A schematic of fundamental SOFC operation is given below in Figure 1.1.

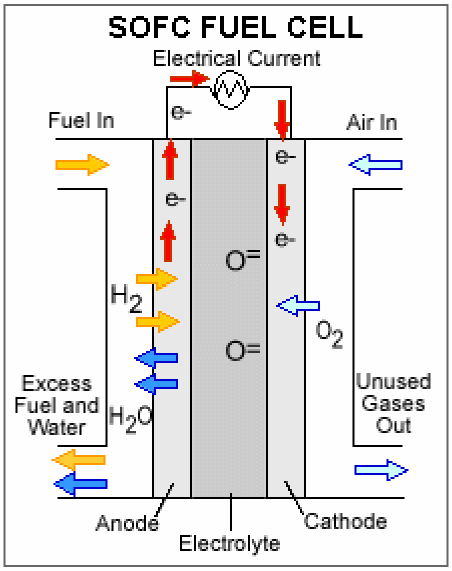
SOFC FUEL CELL
Electrical Current
e-
Fuel In
Air In
e-
e-
e-
O=
H2
O2
O=
Excess Fuel and Water
H2O
Unused Gases Out
Anode
Electrolyte
Cathode

Figure 1.1. Solid oxide fuel cell fundamentals (courtesy of www.eere.energy.gov).

Additionally, there are various unit cell arrangements such as tubular, monolithic, and planar. The latter design, with a co-flow gas channel arrangement, is shown in Figure 1.2 and is conventionally comprised of an anode cermet made of nickel supported upon yttria-stabilized zirconia (Ni-YSZ), an electrolyte that is formed from YSZ, a cathode made of strontium-doped lanthanum manganate (LSM), and a metallic or ceramic interconnect which is used for electrically interconnecting cells to form a stack, as well as providing the gas flow channels for the reactants. As shown in Figure 1.3, the balance-of-plant (b-o-p) of a fuel cell system is comprised of a fuel processing unit, power conditioning section, and an exhaust heat management portion. In the case of the SOFC, the fuel, usually an infrastructural hydrocarbon, may be internally reformed to obtain the needed hydrogen rich mixture, based upon the SOFC's high operating temperature.

Furthermore, the high quality exhaust heat from SOFC b-o-p may be used in a heat engine bottoming cycle [2].

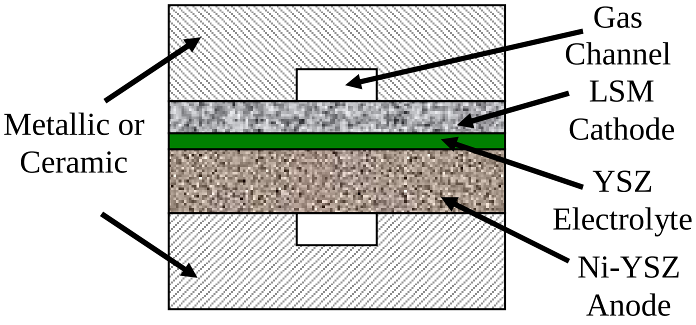
Metallic or Ceramic
Gas Channel
LSM Cathode
YSZ Electrolyte
Ni-YSZ Anode

Figure 1.2. Cross-sectional view of a SOFC unit cell (not to scale).

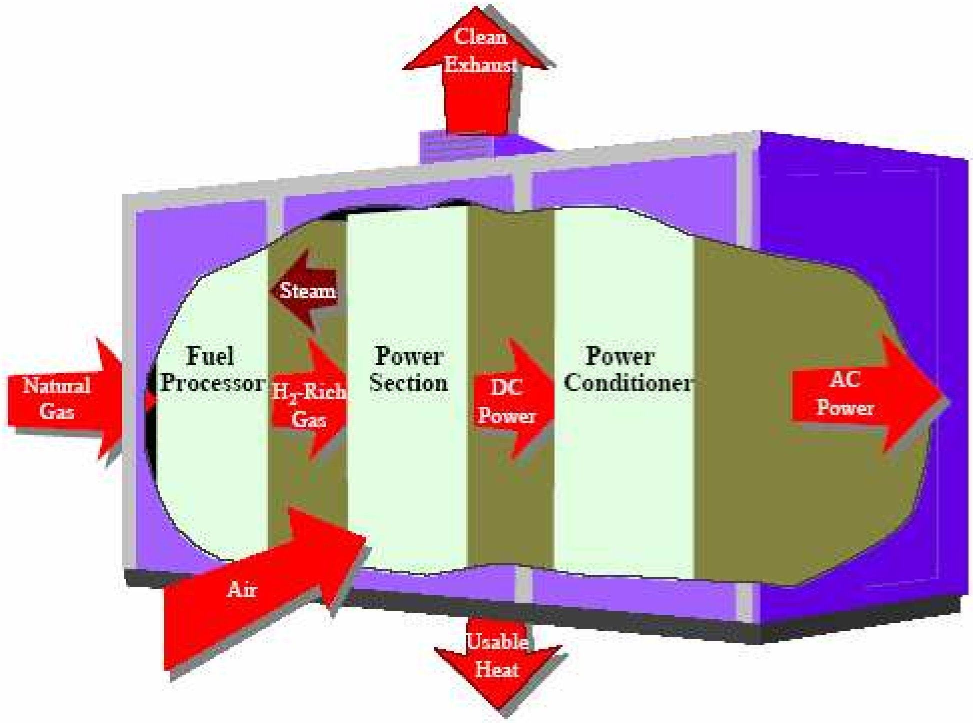
Clean Exhaust
Steam
Natural Gas
Fuel Processor
H_2-Rich Gas
Power Section
DC Power
Power Conditioner
AC Power
Air
Usable Heat

Figure 1.3. Fuel cell system inclusive of stack ("power section") and b-o-p.

In order to facilitate the application of SOFCs, in conjunction with reduced research and development costs, there is a need for accurate performance models to aid scientists and engineers in component and process design. To this end, an enhanced transient performance model has been developed. The present thesis enhances transient modeling and simulation via characterization of two important transient phenomena. They are bimodal stimuli (i.e., simultaneous changes in reactant supply and load demand) electrical transients and the electrochemical light-off phenomenon. The modeling efforts also facilitated complementary modeling and analysis such as electrolysis modeling and assessing the validity of including unsteady anodic mass transfer in electrical transient modeling. Reflective of the state-of-the-art in controls and dynamic simulation development, the modeling efforts are completed in the MATLAB/SIMULINK computing environment. There is then a tangible software development that accompanies the modeling and simulation exercises and transient insights resolved.

The electrical transient model includes a verified steady-state model [3] as its basis, with the inclusion of a Lagrangian approach within the pivotal fuel stream. It should be noted that ability to simulate responses to bimodal stimuli is the major improvement over a previous approach [4]. Simulating bimodal stimuli allows for the uncoupling of the fuel cell from the reactant supply subsystem. This uncoupling is important because the reactant supply subsystem has a time constant typically orders of magnitude greater than that associated with fuel cells [4]. To accommodate this, a fuel ramp time (FRT) was considered. FRT is the time (on the order of seconds) wherein the fuel supply rate is linearly changed from the initial to the final fuel supply rate. It was observed that as FRT increased there is a resulting increase in undershoot or overshoot in both the cell potential and fuel utilization response profiles. Electrical transient simulations of electrolysis were next completed. Electrolysis may occur during a planned (e.g. shutdown) or an unplanned (e.g. a load trip) event, and electrolysis poses potential performance and reliability dangers. The key development was an electrolysis operating map wherein electrolysis was predicted as a function of (initial) fuel utilization and decrease in current demand. Additionally, a time constant analysis was completed wherein the time constant associated with electrical transients was compared to that associated with gas diffusion through the anode. It was observed that at larger initial loads and step changes (e.g. 600 mA/cm^2 and 50% increase) the transient effect of gas diffusion is less impacting upon overarching transient analysis; yet, the results do promote the inclusion of dynamic anodic mass transfer within simulations.

The impetus for a thermal transient model during heat up and load cycling is due to the fact that SOFCs are susceptible to thermal failure caused by the thermal stresses imposed during heat up and cool down (i.e., thermal cycling) of the stack. Cracking ensues in the components, which leads to a decrease in performance and reliability. Therefore, it is imperative that electrically-induced thermal transients be well-characterized for structural and operational design improvement. The key novelty of thermal cycling is the phenomenon termed “electrochemical light off” which is the transitional heating of the cell due to the by-product heat generated due to the electrochemical reactions. Two key results of the electrochemical light off simulations were that electrochemical parameters such as load demand or cell potential may be used as dynamic control variables during transitional heating of the cell; and that there exists an optimum condition for efficient sensible heating of the cell. The electrochemical light off simulations are critical results that will be further extended to modeling thermal transients that occur during changes in load as detailed in the final chapter of the thesis.

CHAPTER 2

LITERATURE REVIEW

Performance models, in general, are predictive tools which help to characterize, gain phenomenological understanding, and assist scientists and engineers in the design of a particular process or system. Any development or enhancement to a performance model will add to each of the aforementioned areas of interest. To this end, an enhanced performance model of a solid oxide fuel cell (SOFC) has been developed and is presented in this thesis. SOFC performance models typically simulate the electrochemistry and the heat and mass transfer. In recent years numerous entities have sought to characterize the performance of a SOFC [4-22]. These performance models may be categorized as either steady-state or dynamic. Within these categories, the performance models may be separated by spatial consideration (i.e. 0-D, 1-D, 2-D, or 3-D), the P-E-N (positive electrode-electrolyte-negative electrode) geometry, P-E-N material set, and modeling approach (e.g., finite element, CFD, etc.). The focus of this literature review is to give an overview of some performance models that characterize electrical performance of SOFC and electro-thermal (e.g. electrochemical light off) considerations during transitional heating of the cell.

Steady-state electrical performance models have been substantially developed [5-14]. Bessette and Wepfer [14] developed a 3-D mathematical model of single cell of a tubular solid oxide fuel cell (TSOFC). In this model, all temperature dependent transport properties were from independent sources and not performance data, and the effects of different oxidants (i.e. air or pure oxygen) and fuels (i.e. carbon monoxide, hydrogen, or both) were quantified. The electrical results were numerically solved via a 3-D discretization of the cell, and the computed heat generation (or loss) from the cell was used by a thermal finite element code. Bessette and Wepfer's electrochemical (and thermal) model was within 5% agreement with single cell test data from a 3kW Siemens (formally Westinghouse) TSOFC which operated in Japan from 1990-1992.

As opposed to a finite element approach, Ferguson, et al., [13] utilized a computationally less arduous finite volume approach in their steady-state performance models of planar, tubular, and monolithic geometries. The performances of a planar SOFC (PSOFC) 1-D co-flow, 1-D counter-flow, and 2-D cross-flow models were compared. The counter-flow model was shown to be the most efficient over a load range of 100-300 mA/cm^2. Ferguson, et al., also used the performance model to determine the optimum (i.e. when designing for cell efficiency) anode thickness for the PSOFC model. The model compared favorably with the benchmark set by the International Energy Agency.

Haynes and Wepfer [12] developed a steady state performance 1-D model of a TSOFC based upon an axial discretization methodology shown in Figure 2.1. This method utilized a potentiostatic approach. Moreover, the cell voltage is considered a uniform boundary condition and the 'slice' current is converged upon after solving a set of transcendental equations. A computational 'marching' through the slices is completed until the end of the cell is reached thereby characterizing the electrical performance of the cell. This model proved to be a useful tool in optimizing cell for power in terms of operating conditions such as fuel stream chemistry effects (i.e. shift equilibrium and anode recirculation), anode thickness (i.e., for a PSOFC), fuel utilization effects, and operating pressure. This model was validated with experimental data from Siemens (Siemens Westinghouse at the time) to within 3% agreement.

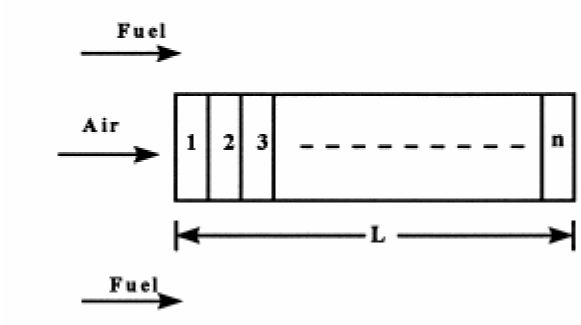

Figure 2.1. Discretization methodology that facilitated the 1-D performance model of a TSOFC by Haynes and Wepfer [12].

There are two other conventional methodologies of modeling the performance of a SOFC which are an equivalent circuit method and a computational fluid dynamics (CFD) approach. An equivalent circuit method is utilized by Iwata et al., [11] and Li et al., [7] wherein the voltage and current distribution is calculated using Kirchhoff's Law as shown in Figure 2.2 and Figure 2.3. Larrain et al., and Sudaprasert et al., [5, 6] a CFD approach wherein user-defined electrochemistry code or electrochemistry modules are used in the CFD software Fluent and STAR-CD, respectively. Nonetheless, each particular method has its advantages and disadvantages in predicting the performance of SOFCs. The use of CFD software such as Fluent or STAR-CD offers modeling convenience in terms of solving the heat transfer and fluid dynamics governing equations. CFD software also provides higher fidelity than a equivalent circuit method. However, these software packages do not include the electrochemistry code and can take enormous amounts of time to run a simulation (on the order of 1 day). What is lost in terms of fidelity in equivalent circuit modeling approach is gained in computational simplicity and speed.

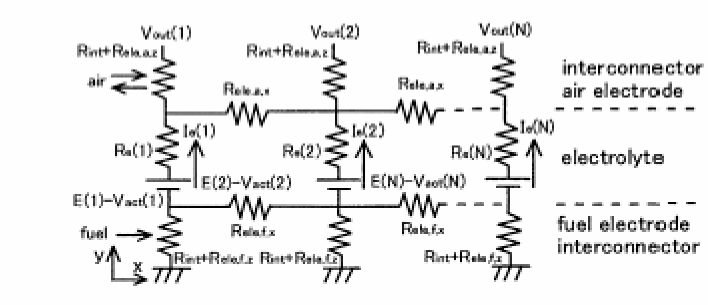
Vout(1)
Vout(2)
Vout(N)
Rint+Rele,a,z
Rint+Rele,a,z
Rint+Rele,a,z
air
Rele,a,x
Rele,a,x
interconnector
air electrode
Ie(1)
Ie(2)
Ie(N)
Re(1)
Re(2)
Re(N)
electrolyte
E(2)−Vact(2)
E(N)−Vact(N)
E(1)−Vact(1)
fuel
Rele,f,x
Rele,f,x
fuel electrode
interconnector
y
x
Rint+Rele,f,z
Rint+Rele,f,z
Rint+Rele,f,z

Figure 2.2. Equivalent circuit method to solve for voltage and current distributions within a PSOFC [11].

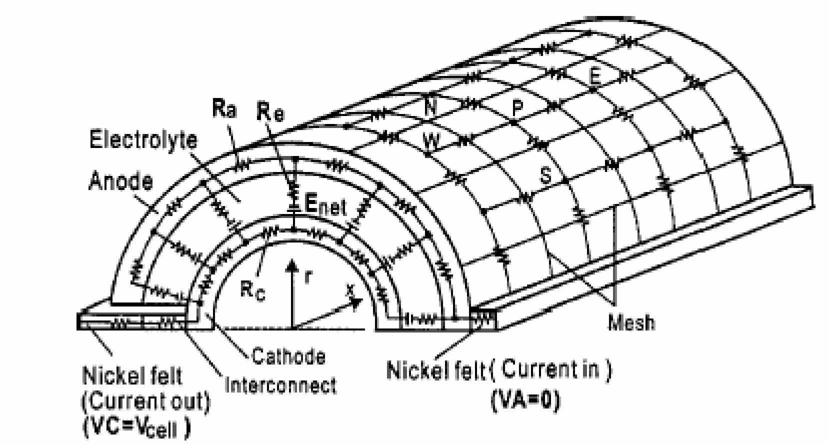
Ra
Re
Electrolyte
Anode
N
P
E
W
S
Enet
Rc
r
x
Mesh
Cathode
Interconnect
Nickel felt
(Current out)
(VC=Vcell)
Nickel felt(Current in)
(VA=0)

Figure 2.3. Equivalent circuit method for a TSOFC to solve for voltage and current distributions [7].

As noted by Brandon et al. [15], far more steady-state performance models of SOFCs have been produced relative to the number of dynamic models. One of the first dynamic models of SOFC was produced by Achenbach [16, 17]. Achenbach's developed a 3-D model of a PSOFC wherein electrochemistry, mass, and energy equations were numerically solved. The model accounted for methane steam reforming, the water-gas-shift reaction, temperature-dependent polarization terms (i.e. activation, ohmic, and concentration), and heat transfer via conduction, convection, and radiation. There are two key results of Achenbach's work that are particularly relevant to the present thesis.

The first is the simulation of load changes (i.e. with invariant fuel and oxidant supply) and its effect on voltage and temperature transient profiles. Achenbach observed an undershooting of the final steady-state voltage when the load was increased (i.e. a step change). The second key result is the observation that changes in load demand stimulate thermal transients. It was observed that when the load increased that cell temperature would increase to a new steady-state temperature over a period of minutes.

Haynes [4], like Achenbach, simulated the electrical and thermal transients due to a change in current demand considering an invariant fuel and oxidant supply rate. However, Haynes utilized a Lagrangian modeling approach wherein each fluid element is tracked spatially and temporally as shown in Figure 2.4. This "slice" technique facilitated simulation of both electrical and thermal responses in a TSOFC. However, the code did not consider the possibility of simultaneous stimuli (i.e. current and fuel supply rate changes).

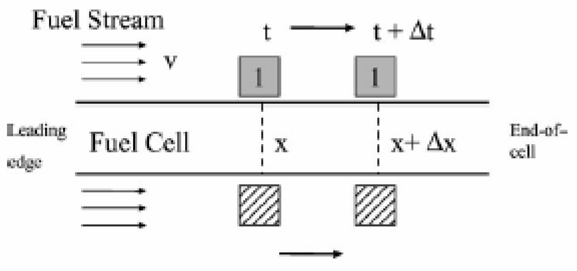

Figure 2.4. Lagrangian approach showing the connection between spatial and temporal discretization [4].

Brandon al. [15] present a 1-D co-flow PSOFC model that is an extension of their steady-state performance code [10]. In their model a developed set of algebraic and partial differential equations which describe the electrochemistry and energy balance of a cell are solved using *gPROMS ModelBuilder 2.2.5* software combined with a finite difference integration approach. This model was used to illustrate both open and closed loop responses in voltage and temperature profiles to load changes in a SOFC. The model, however, is designed to control current while setting the fuel supply rate proportional to the current change (i.e. fixed fuel utilization control of fuel supply rate) and does not allow for possibly *delayed* reactant supply rate changes, which impact electrical transients.

Sedghisigarchi and Feliachi [18] developed a dynamic 0-D bulk SOFC model in the MATLAB/SIMULINK computing environment which considered species dynamics and heat transfer . Sedghisigarchia and Feliachi simulated dynamic responses of the cell potential and temperature to step changes in load and fuel flow. However, their work failed to consider the scenario wherein changes occurred in both the load demand and fuel supply rate (i.e. bi-modal stimuli). Such a scenario is possible in a 'slaved' situation wherein the fuel processor is slower than the power electronics fuel cell subsystems [4].

Electrochemical light off is the latter stage transitional heating of the SOFC stack to a desired operating temperature during which heat may strategically be generated from the electrochemical reactions. The electrochemical light off phenomenon has not been *explicitly* studied in the open literature. However, a few groups [17], [19, 20] have modeled the thermal transients that occur during start up of a SOFC.

Achenbach [17] did consider the start up event of SOFC operation, however, it was deemed as a special case of a load change. Whereas, Damm and Fedorov [19, 20] give more detail in terms their treatment of the heat transfer. More specifically, they considered 2-D effects and take into account conduction, convection, and radiation. The results of the model compared well to a CFD code developed in Fluent. However, they do not consider the heat generation source term that is due to the exothermic electrochemical reactions. On the contrary, Petruzzi, et al., [21] and Khaleel et al., [22] have developed a coupled thermo-electrochemistry model that simulate start up of a SOFC. Pertruzzi's model is developed in the MATLAB programming language and was used primarily as a tool for assessing the time for heat up of a stack, characterizing temperature gradients (i.e. which lead to thermal stresses), and to develop a pre-operating strategy. The electrochemical model utilizes an equivalent circuit within finite volume approach (i.e. 1-D model for each cell). The heat generation profile from the electrochemical model is used in a 3-D thermal model (i.e. stack model). Although, the code was designed to offer a pre-operating strategy to mitigate possible material failure during transitional heating, the work only considered the air flow as a possible parameter to control the heat; there was no rigorous consideration of the electrochemical operating conditions (i.e. electrochemical light off phenomenon). Khaleel, et al., [22] used 3-D finite element (FE) code, MARC, which was combined with a electrochemical module to simulate the start up of a cell. The model did not offer any results showing the impact of electrochemical operating conditions on cell heat up. The MARC FE code is computationally stable and more efficient (i.e. CPU time vs. number of cells) than that of the CFD STAR-CD code. All in all, the ultimate goal of a dynamic thermo-electrical model should be to characterize cell operation accurately (i.e. inclusive of all relevant phenomena such as heat generation), yet be computationally efficient.

While performance models of SOFCs is an active area of research especially in recent years with the improvement of computational tools, there are some enhancements that can be made to the state-of-the-art. In particular, further enhancements to electrical transients and thermo-electrical models such as bi-modal stimuli response and electrochemical light off, respectively, would be worthwhile additions. The ability to simulate bi-modal stimuli is a clear area of need within the SOFC modeling community wherein electrical response to a change in load demand and/or reactant supply rates is pivotal. Finally, the electrochemical light off phenomenon has not been extensively investigated. Specifically, the present literature has not reported the impact of electrochemical operating conditions on transitional heating of the cell.

CHAPTER 3

ELECTRICAL TRANSIENTS WITHIN SOFCS

3.1 SOFC operation

3.1.1 Chemistry and Electrochemistry Associated with the SOFC

The SOFC converts chemical energy into electrical energy by electro-oxidizing hydrogen and electro-reducing oxygen (from air), and then routing the free electrons to an external load thereby producing electricity. The hydrogen and oxygen anions react at the anode to produce water as shown in Equation (3.1) below. Due to the fuel processing of the fuel (e.g. methane via steam reformation), carbon monoxide may be present in the fuel stream. Carbon monoxide may also react with the oxygen anions to promote electricity as shown in Equation (3.2).

$$2H_2 + O^{-2} \rightarrow 2H_2O + 4e^- \tag{3.1}$$

$$2CO + O^{-2} \rightarrow 2CO_2 + 4e^- \tag{3.2}$$

These reactions also produce high quality thermal energy and do not consume all of the fuel as detailed in the control volume highlighted in Figure 3.1 Due to the high temperature regime of a SOFC, “light” hydrocarbons such as methane may be internally reformed. Methane is reformed with gaseous water to produce carbon monoxide and hydrogen as detailed in Table 3.1. The carbon monoxide may then be taken through a "water-gas shift" reaction to produce carbon dioxide and hydrogen which is shown in Table 3.1. The hydrogen from reformation and the water-gas shift reaction will then react with oxygen anions to promote electricity, steam, and heat. The stated chemical and electrochemical reactions are described in Table 3.2. For the present thesis, it is presumed that the water-gas shift reaction is favored over the direct oxidation of carbon monoxide [12].

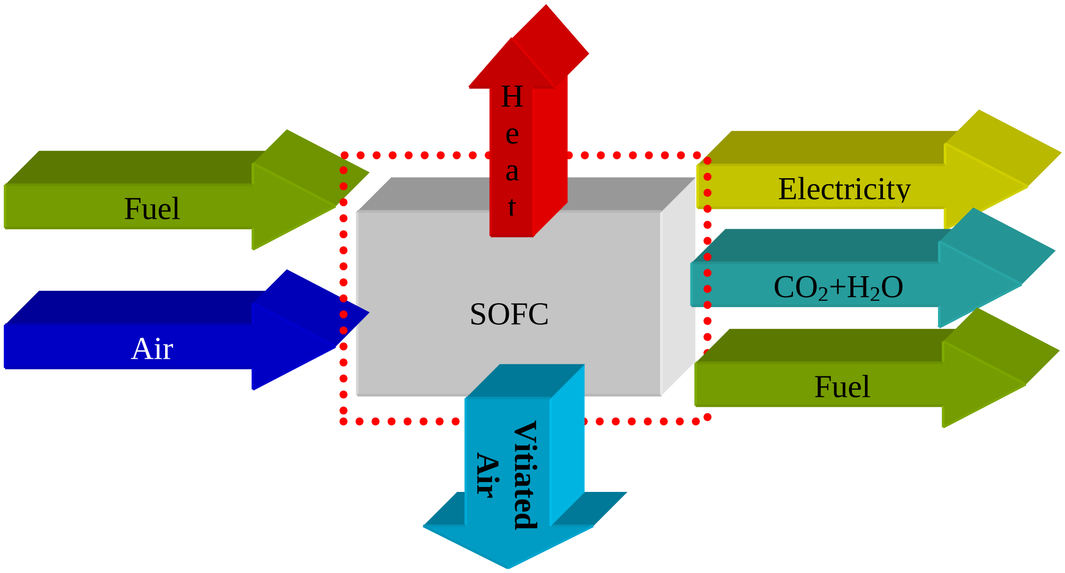

Figure 3.1. Control volume for the analysis of a solid oxide fuel cell. (Note that lengths of the arrow do not indicate relative amount or value.)

Table 3.1. Chemical Reactions for methane reformation SOFC.

Methane Reformation	$CH_4 + H_2O \rightarrow CO + 3H_2$ (3.3)
Water-Gas Shit Reaction	$CO + H_2O \rightarrow CO_2 + H_2$ (3.4)

Table 3.2. Electrochemical reactions for SOFC operation.

Anode Reaction	$2H_2 + 2O^{-2} \rightarrow 2H_2O + 4e^-$ (3.5)
Cathode Reaction	$O_2 + 4e^- \rightarrow 2O^{-2}$ (3.6)

3.1.2 Nernst Potential

The Nernst potential is directly proportional to the maximum useful work that can be derived from an electrochemical device. This relationship between Nernst potential and useful work may be summarized in the following equation

$$W_{\max} = nFE \tag{3.7}$$

where n is the number of electrons transferred per mole of fuel, F is Faraday's constant (96485 coulombs), and E is the Nernst potential. Furthermore, the maximum useful work can be described by applying the first and second laws of thermodynamics (neglecting changes in potential and kinetic energy), which is characterized by the decrease in Gibbs free energy for an open system (e.g., SOFC).

$$W_{\max} = \sum_{reactants} n_i G_i - \sum_{prducts} n_j G_j \tag{3.8}$$

It can be assumed that the fluid stream's constituents are ideal gases hence allowing the associated Gibbs free energy (i.e., chemical potential) to be expressed in terms of absolute temperature and pressure relative to standard conditions.

$$G_k = G_k^{\circ} + R_u T \ln(p_k) \tag{3.9}$$

Note that in Equation (3.9), R_u is the universal gas constant and p_k is the constituent's dimensionless partial pressure (i.e., partial pressure normalized by the standard pressure). Using the preceding three equations, the Nernst potential is therefore implicitly related to the decrease of Gibbs free energy as expressed in the following equation.

$$nFE = \sum_{reactants} n_i \left[G_i^{\circ} + R_u T \ln(p_i)\right] - \sum_{prducts} n_j \left[G_j^{\circ} + R_u T \ln(p_j)\right] \tag{3.10}$$

For the general chemical reaction:

$$\alpha A + \beta B \rightarrow cC + \delta D \tag{3.11}$$

Eqn. 10 becomes:

$$nFE = -\Delta G^{\circ} - R_u T \ln\left[\frac{p^c p^{\delta}}{p^{\alpha} p^{\beta}}\right] \tag{3.12}$$

where the first term of Equation (3.11) is the *decrease* in Gibbs free energy. The general form of the Nernst equation, for an ideal gas reaction, is thus given by:

$$E = \frac{-\Delta G^{\circ}}{nF} - \frac{R_u T}{nF} \ln\left[\prod_i p_i^{\nu_i}\right] \tag{3.13}$$

where ν_i is the stoichiometric coefficients of the constituents. Applying the general form of the Nernst equation to SOFC operation wherein hydrogen is oxidized yields the following:

$$E = \frac{-\Delta G^{\circ}_{H_2 \rightarrow H_2O}}{2F} - \frac{R_u T}{2F} \ln\left[\frac{p_{H_2O}}{p_{H_2}\, p_{O_2}^{1/2}}\right] \tag{3.14}$$

3.1.3 Typical V-J Performance Curve

Solid oxide fuel cells, like any energy conversion device, performs non-ideally due to irreversibilities. This deviation from Nernst potential or ideal voltage is captured on what is called a polarization curve as shown in Figure 3.2.

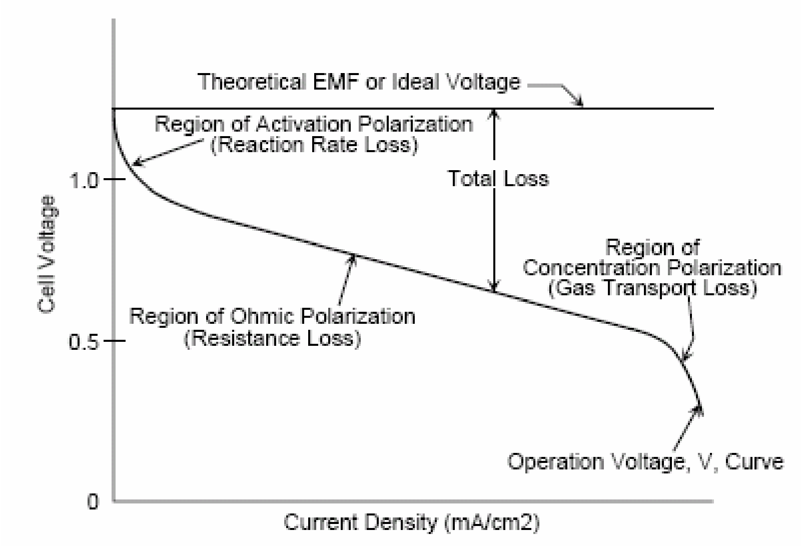

Figure 3.2. Polarization curve showing the various loss mechanisms (i.e. polarizations) that occur during fuel cell operation [23].

As shown in Figure 3.2, there are three types of polarizations and regions of operation wherein a particular loss mechanism is dominant relative to the other polarizations. At and near open circuit voltage (low current densities), activation polarization is the dominant loss term. Activation polarization is attributed energy required to sustain the electrochemical reactions. At intermediate current densities, ohmic voltage decrease is the dominant loss mechanism. Ohmic losses obey Ohm's Law in terms of proportionally increasing as current increases. Ohmic losses are associated with the resistance (i.e. area-specific-resistance or ASR) mainly caused by the electrolyte and interfacial surfaces. At higher current demands, concentration polarization is the dominant overpotential. Concentration losses are attributed to mass transport effects that cause a reactants partial pressure drop in both electrodes thereby decreasing cell potential. More detail of each loss mechanism will be discussed in the following section. Subtracting the three polarizations from the Nernst potential yields the operating voltage of a fuel cell as shown in the following equation:

$$V = E - V_{ohmic} - V_{act} - V_{conc} \tag{3.15}$$

where E is Nernst potential, V_{ohmic} is the ohmic loss, V_{act} is the activation polarization, and V_{conc} is the concentration polarization

3.1.4 Further Detail and Modeling Regarding Each Loss Mechanism

As was previously introduced, there are three primary loss mechanisms in SOFCs—activation and concentration polarizations, and ohmic losses. Each will be discussed in further detail. It should be noted that in the electrical transient model, activation and concentration polarization losses were modeled based upon Bard and Faulkner [24] and the work of Kim et al. [25]. Due to the proprietary nature of fuel cells, there is limited published data of the various polarizations; therefore, numerical curve fits taken from the work of Kim et al. [25] were used to model the polarization loss mechanisms in this representative modeling activity.

Activation polarizations are attributed to the energy barrier that the electrochemical reactions must overcome in order for electricity to be produced. At open circuit voltage (OCV), each electrode is in dynamic equilibrium thereby developing a potential difference. The dynamic equilibrium of each electrode at OCV is maintained by the balanced electrochemical free energies. More specifically for SOFCs, hydrogen is electro-oxidized to produce steam, and oxygen is ionized, as shown below.

$$2H_2 + 2O^{-2} \leftrightarrow 2H_2O + 4e^- \tag{3.16}$$

$$O_2 + 4e^- \leftrightarrow 2O^{-2} \tag{3.17}$$

The electrochemical free energies are the combination of the chemical and the electric work potential associated with the de-ionization and ionization of hydrogen and oxygen. Therefore, the electrochemical "half cell" reactions produce continual gross flows of electrons to and from the electrolyte-electrode interfaces [2]. As a result, a gross current is developed which is known as the exchange current density. When the electrode kinetics are "sluggish" the exchange current density is low; therefore, the Tafel equation is used to relate exchange current density to the activation polarization as shown below

$$V_{act} = a + b \ln i'' \tag{3.18}$$

a and b are defined in the equation below.

$$a \approx -\frac{R_u T}{4\alpha F} \ln i_o \tag{3.19a}$$

$$b \approx -\frac{R_u T}{4\alpha F} \tag{3.19b}$$

In Equations (3.18) and (3.19), i is the current density and α is the charge transfer coefficient. The charge transfer coefficient is an experimentally determined constant (i.e. function of material with a value between 0 and 1) and is the proportion of the electrical energy applied that is consumed in changing the rate of the electrochemical reaction. It should be noted that activation polarization is a function of temperature and therefore is minimized in SOFCs because of the high operating temperature.

For a temperature range of 650-800°C, the activation polarization was quantified using a curve fit of the data of Kim et al. [25]. Hence, the following relationships were developed for the constants a and b of Equation (3.19).

$$a = 23.8335 - 6.86 \cdot 10^{-2} T + 6.6023 \cdot 10^{-5} T^2 - 2.12 \cdot 10^{-8} T^3 \tag{3.20a}$$

$$b = -4.38865 + 1.37 \cdot 10^{-2} T - 1.40852 \cdot 10^{-5} T^2 \tag{3.20b}$$

Ohmic losses are the dominant loss mechanism at intermediate current densities. These losses are due to the resistance to the flow of ions across the electrolyte and electrons across the electrodes and interconnects. Since these losses obey ohm's law, the experimentally determined parameter, ASR, is used to account for this loss. Therefore, ohmic losses are modeled in the following equation.

$$V_{ohmic} = i''\cdot R_i \tag{3.21}$$

ASR is given as R_i in the equation above. ASR is a function of the effective resistivity and path length of the material (i.e. primarily the electrolyte thickness), and is dependent upon operating temperature.

The temperature dependency of ASR for a *unit cell* was modeled using, again, Kim et al. [25] as a reference. However, full cell and *stack* ASR values are usually approximately an order of a magnitude larger than that of unit cells. Therefore, the curve fit of Kim et al. data was multiplied by a factor of ten and was utilized in the electrical transient model as shown below.

$$R_i = 10\cdot\left(1.5e-6\cdot T^2 - 0.003748\cdot T + 2.361065\right) \tag{3.22}$$

Concentration polarizations become more prevalent at higher current densities. This is a result of the mass transport limitations in each electrode thereby creating a limiting current density for both the cathode and anode. Such a scenario is depicted in Figure 3.3.

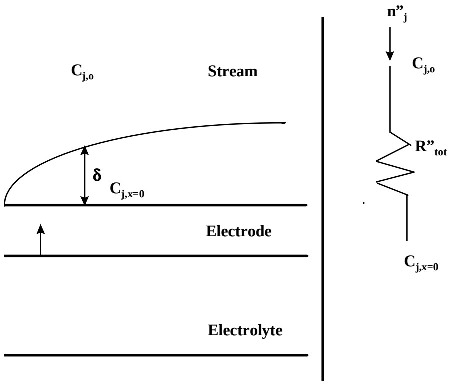

Figure 3.3. Diagram of the mechanism of concentration polarization stemming from a limiting current [14].

By Faraday's Law, this limited current density may be quantified. Faraday's Law describes is the relationship (i.e. based on conservation of mass for a specie) between current produced by an electrochemical reaction relative to the molar flow rate of a reactant.

$$i = \frac{nF}{v_j} \cdot \dot{n}_j \qquad \text{(Faraday's Law for a single cell)}$$

Note that $\dot{n}_j$ is the consumption/production rate of a specie, nF is the charge transfer per mole, and v_j is the stoichiometric coefficient (e.g., in the reaction $H_2 + 0.5\ O_2 \rightarrow H_2O$, where v_{H_2} = -1, v_{O_2} = -0.5, and v_{H_2O} = 1). In the limiting case (i.e. the current at which a constituent is consumed/produced at a maximum rate), the following equation describes the limiting current density in accordance to Faraday's law.

$$i_{l,j} = \frac{nF}{v_j} \cdot \frac{C_{j,o}}{R_{mass,transfer}} \qquad (3.23)$$

where $C_{j,o}$ is the concentration of a reactant in the free stream, and $R_{mass,transfer}$ is the mass transfer resistance. Recall Equation (3.13) where the Nernst potential was given as the following.

$$E = \frac{-\Delta G^\circ}{nF} - \frac{R_u T}{nF} \ln\left[\prod_i p_i^{v_i}\right] \qquad \text{(Recasting of 3.13)}$$

As reported by Haynes [12], based upon Equation (3.13) that the concentration polarization term may be modeled in the following manner.

$$V_{conc} = \frac{R_u T}{nF} \cdot \ln\left[\prod_{\text{reactants}} \left[1 - \frac{i"}{i_{i,j}}\right]^{v_j}\right] \qquad (3.24)$$

Applying this formulation to the present scenario and using the work of Kim et al. [25], the following relationships were used to describe the magnitude of concentration polarization.

$$V_{conc} = -\frac{R_u T}{2F}\ln\left[1-\frac{i''}{i_a}\right]+\frac{R_u T}{2F}\ln\left[1+\frac{p_{H_2}\cdot i''}{p_{H_2O}\cdot i_a}\right]-\frac{R_u T}{4F}\ln\left[1-\frac{i''}{i_c}\right] \quad (3.25)$$

$$i_a = \frac{2F\cdot p_{H_2}\cdot 10.1325\cdot D_{a,eff}}{R_u\cdot 100\cdot T\cdot l_a} \quad (3.26)$$

$$i_c = \frac{4F\cdot p_{O_2}\cdot 10.1325\cdot D_{c,eff}}{\left[1-\frac{p_{O_2}}{p}\right]R_u\cdot 100\cdot T\cdot l_c} \quad (3.27)$$

In Equations (3.26) and (3.27), $D_{a,eff}$ and $D_{c,eff}$ are the effective binary diffusion coefficients, and l_a and l_c are the electrode thickness for anode and cathode, respectively.

3.2 Electrical Transients Model

3.2.1 Motivation

There is an apparent need for reduced research and development costs. Therefore, accurate performance models are needed to aid scientists and engineers in component and process design. To this end, an enhanced electrical transients performance model has been developed.

Electrical transients occur when load changes are demanded by the power electronics (e.g., during start-up) and/or when reactants supply rates change. Often, the power electronics and reactants supply subsystems are slaved together (i.e. transient response is synchronous). Under load-following conditions, this is undesirable primarily due to longer time constants associated with fuel processors [4]. Furthermore, there have been few modeling efforts which have characterized an uncoupled dynamic response of SOFC as was mentioned in the literature review. Therefore, it was desired to simulate a scenario wherein both the load demand and the reactants supply rate were changed simultaneously (i.e. bi-modal stimuli). Hence, a major modeling enhancement over a previous approach [3] is the ability to simulate "unslaved" cell/stack response to bi-modal stimuli.

3.2.3 Model Algorithm

To facilitate the simulation of the electrical response to bi-modal stimuli, the electrical transient model utilized a Lagrangian approach. The core tenet of the Lagrangian approach is that, although *electrochemical* transient responses are short-lived in comparison to thermal-hydraulic transients, longer *electrical* transient effects still arise due to changes in reactant streams' concentrations. The reactant stream fluid elements involved in the transient episodes are computationally "tracked." This was done via two-dimensional arrays containing *field variable* information (i.e., axial position and time). The Lagrangian basis is that a fluid element occupies a certain location at a given time.

$$\eta_{element,fluid} = \eta(\bar{x}, t) \tag{3.28}$$

The symbol η represents the properties of the fluid element in question (e.g., constituent partial pressures). The electrical power produced along the cell depends upon these properties. In accordance with the Lagrangian methodology, the axial discretization (i.e., slice length) is compliant with the *fuel stream* flow velocity and the temporal discretization (i.e., desired simulation time step) of the cell. It is assumed that the fuel stream effects dominate those of the oxidant stream. The reason for selecting the fuel stream flow velocity is due to the fact that the oxidant is supplied in large excess for thermal management. Therefore, oxidant utilization is not as sensitive to stimuli such as changes in current. Figure 3.4 and the following equation conceptually illustrate the discretization.

$$\Delta\vec{x} = \vec{v}\Delta t \qquad \text{(Discretization Length)}$$

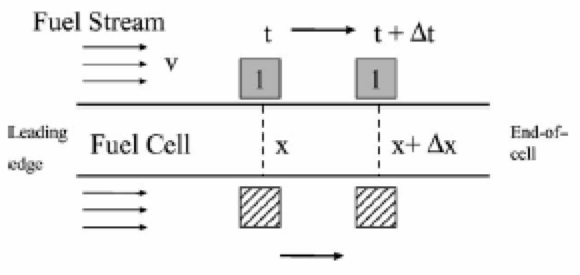

Figure 3.4. Illustration of the discretization of the cell which is a key aspect of the electrical transients modeling approach [4].

The Reynolds Transport Theorem is now utilized, and the following relation results.

$$\eta_{fluid,element}(t+\Delta t) = \eta(\vec{x}+\Delta\vec{x}, t+\Delta t) \tag{3.29}$$

Further consideration is given specifically to molar flows of constituents through simulated “slices” (i.e., axial increments) along the cell.

$$\dot{n}_{\text{j,intermed}}\left(\vec{x}+\Delta\vec{x}, t+\Delta t\right) = \dot{n}_{j,entering,slice}\left(\vec{x}, t\right) + \Delta\dot{n}_j\left(\vec{x}, t\right) \tag{3.30}$$

The “j” subscript represents primary constituents hydrogen, oxygen and steam, and Equation (3.30) accounts for the temporal change in constituents due to electrochemical oxidations as governed by Faraday's law shown below.

$$\Delta\dot{n}_j\left(\vec{x}, t\right) = \frac{v_j \cdot i_j}{nF} \tag{3.31}$$

The quasi-steady state electrochemistry assumption is incorporated, meaning that electrochemical phenomena occur as if at steady state, at the given instant. Given a reformate stream mixture, the shift reaction is also considered.

$$\dot{n}_k(\vec{x}+\Delta\vec{x}, t+\Delta t) = \dot{n}_{\mathrm{k,intermed}}\left(\vec{x}+\Delta\vec{x}, t+\Delta t\right) + \dot{n}_{k,shift,change}\left(\vec{x}, t\right) \qquad (3.32)$$

The "k" subscript represents hydrogen, steam, and, if present, carbon monoxide and carbon dioxide. Equation (3.32) accounts for the temporal changes in constituents due to the shift reaction (Equation (3.4)), which was modeled via equilibrium chemistry [12] due to the high temperature fuel stream and nickel catalyst within the anode. The equilibrium constant is then expressed as follows.

$$K_{shift}(T) = \frac{p_{H_2}\, p_{CO_2}}{p_{H_2O}\, p_{CO}} \qquad (3.33)$$

Due to an equal number of moles of the shift reaction, pressure does not influence the equilibrium condition of the reaction. Therefore, Equation (3.33) may be recast in the following manner.

$$K_{shift}(T) = \frac{\dot{n}_{H_2}\, \dot{n}_{CO_2}}{\dot{n}_{H_2O}\, \dot{n}_{CO}} \qquad (3.34)$$

Winnick [26] provides a relationship for the shift equilibrium constant.

$$K_{shift}(T) = \exp\left(\frac{-\Delta G_{shift,reaction}}{R_u T}\right) \qquad (3.35)$$

Winnick [26] also provides a quadratic equation which may be solved to account for changes in molar flow rate due to the shift reaction as denoted in Equation (3.32). These temporal expressions of mass conservation enabled the transient electrochemical model to "march out" in time.

Figure 3.5 shows the algorithm of the transient electrochemical model. At the beginning of each simulation, the initial and final steady-state operating points are generated, and they provide overarching end points for the simulated transient event. As collectively shown in the “Input Packet Data” parallelogram of the flow chart of Figure 3.5, the transient model receives parameters that simulate relevant balance-of-plant (b-o-p) components (e.g. fluidic and electrical settings), cell properties (e.g. unit cell dimensions, stack geometry, and material properties), and operating conditions for each temporal "packet." A packet is defined as a condition wherein the reactant supply rates are presumed static over a prescribed timeframe of the simulation. The use a packet methodology was to simulate changes in reactant supply rate and/or current profile. This is the key tenet which facilitated the ability to simulate bi-modal stimuli. Within a packet, the prescribed current density is converged upon via the bracketed *Regula Falsi* method for robustness and computational speed. Since voltage is a uniform boundary condition, voltage is adjusted for each iteration and the *average* current density (i.e. sum of each slice current density) is compared to the prescribed current density as illustrated in Figure 3.5. After current density is converged upon, the constituent molar flow rates, mole fractions, and partial pressures are updated.

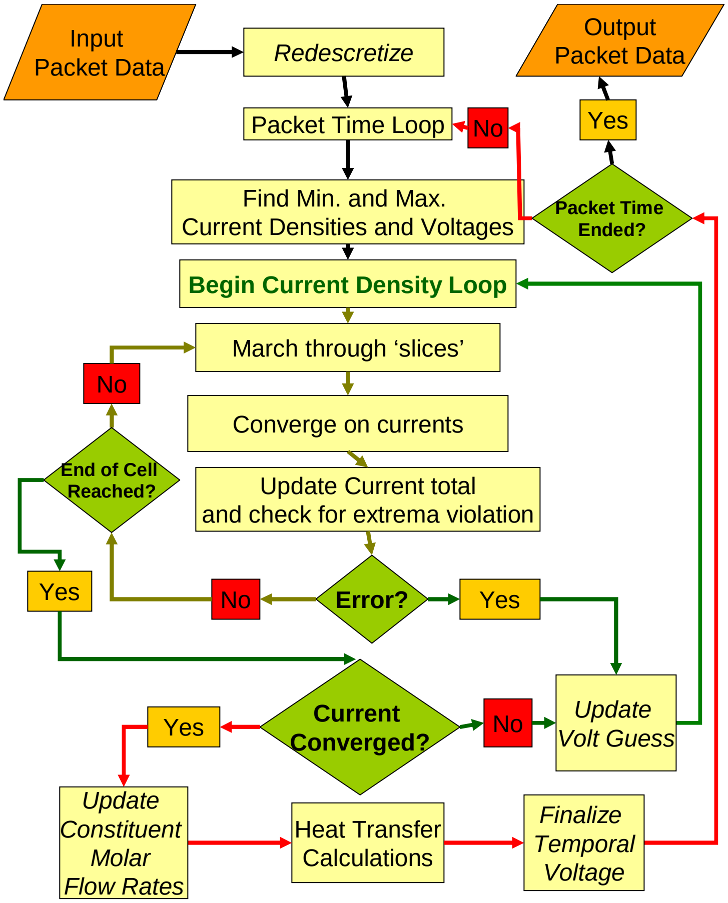
Input Packet Data
Redescretize
Output Packet Data
Packet Time Loop
No
Yes
Find Min. and Max. Current Densities and Voltages
Packet Time Ended?
Begin Current Density Loop
March through 'slices'
No
Converge on currents
End of Cell Reached?
Update Current total and check for extrema violation
Yes
No
Error?
Yes
Yes
Current Converged?
No
Update Volt Guess
Update Constituent Molar Flow Rates
Heat Transfer Calculations
Finalize Temporal Voltage

Figure 3.5. Electrical transients model flowchart ("Intra-packet" level).

At the end of each packet, the transient data (e.g., constituent mole fractions distribution) is passed to the next packet as shown in Figure 3.6. This process is continued for a predetermined amount of time, which is typically five simulated seconds (i.e. electrical transient response is on the order of seconds).

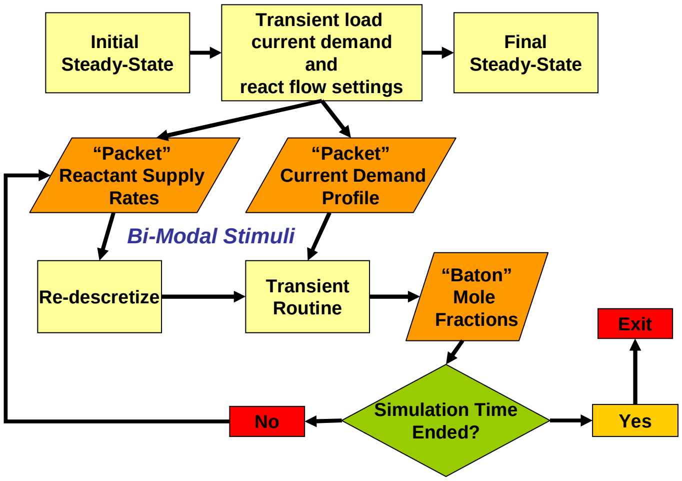
Initial Steady-State
Transient load current demand and react flow settings
Final Steady-State
"Packet" Reactant Supply Rates
"Packet" Current Demand Profile
Bi-Modal Stimuli
Re-descretize
Transient Routine
"Baton" Mole Fractions
Exit
Simulation Time Ended?
No
Yes

Figure 3.6. Electrical transients model algorithm ("Inter-packet" level).

To further elucidate the modeling algorithm, a numerical example is presented. Consider the initial and final steady-state conditions described in the Table below.

Table 3.3. Initial and final steady-state conditions for a transient simulation.

Parameter	**Initial**	**Final**
Current Density (mA/cm^2)	350	600
Fuel Utilization (%)	50	70
Fuel Supply Rate (mmol/sec)	0.0453	0.0555
Number of Slices (Δt = 4 msec)	387	316

Consider also a simulation time of five seconds with 0.1 per packet, and a step change in current density and fuel supply rate. Since the number of slices changes between the initial and final steady state conditions, the constituent mole fractions distribution must be rediscretized for the first packet. After the first packet, the baton mole fractions are passed to the next packet as illustrated in Figure 3.6. Since the fuel supply rate and corresponding number of slices remain constant for the remaining 4.9 seconds of simulation time, rediscretization is not required. Although the fuel supply rate will not change for the rest of the simulation, the mole fractions will change (i.e. fuel stream composition). The changes in fuel stream composition are caused by the electrochemical oxidation and the water-gas shift reaction.

More discussion regarding rediscretization is offered. As shown in algorithm in Figure 3.6, the ability to simulate bi-modal stimuli is a key feature of the algorithm. Recall that the axial discretization is a function of time increment and fuel stream velocity as was previously described.

$$\Delta\vec{x} = \vec{v}\Delta t \qquad \text{(Discretization Length)}$$

The number of slices for a packet may vary from packet to packet, as a function of variable fuel supply rates. Therefore, a rediscretization of the packet mole fractions was developed in order to accommodate changing slice counts. Consider the situation where initially the number of discretized slices is 4 (typically on the order of 100-1000 slices, but an artificially small number is herein used for simplicity). A change in current demand or fuel supply rate dictates that the next packet will have 5 slices in the packet. Therefore, the hydrogen mole fractions must be redistributed over the 5 slices while maintaining the boundary conditions and the profile of the original distribution as shown in Figure 3.6. A cublic spline methodology was used to redistribute the mole fractions at the beginning of each packet.

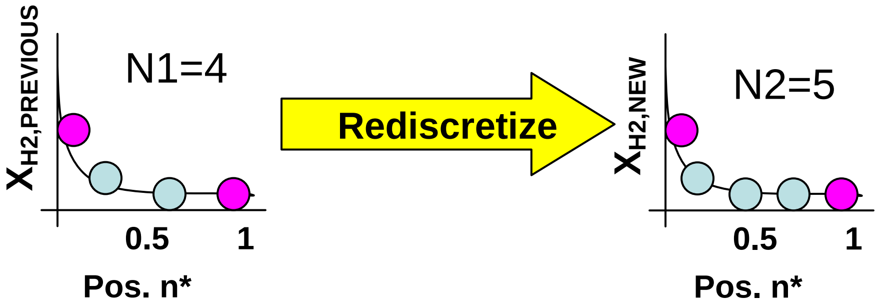

Figure 3.7. Illustration of the rediscretization solution of the mole fraction distribution problem that arises when the number of slices changes due to a change in fuel flow rate.

3.2.4 Sample Electrical Transient Results and Discussion

A sample plot of the ability to simulate bi-modal stimuli is given in Figure 3.7. Three simulations were performed wherein an instantaneous step change in current demand occurred while the fuel ramp time (FRT) was varied using zero, one, and three seconds. FRT is the time wherein the fuel supply rate is linearly changed from the initial to the final fuel supply rate.

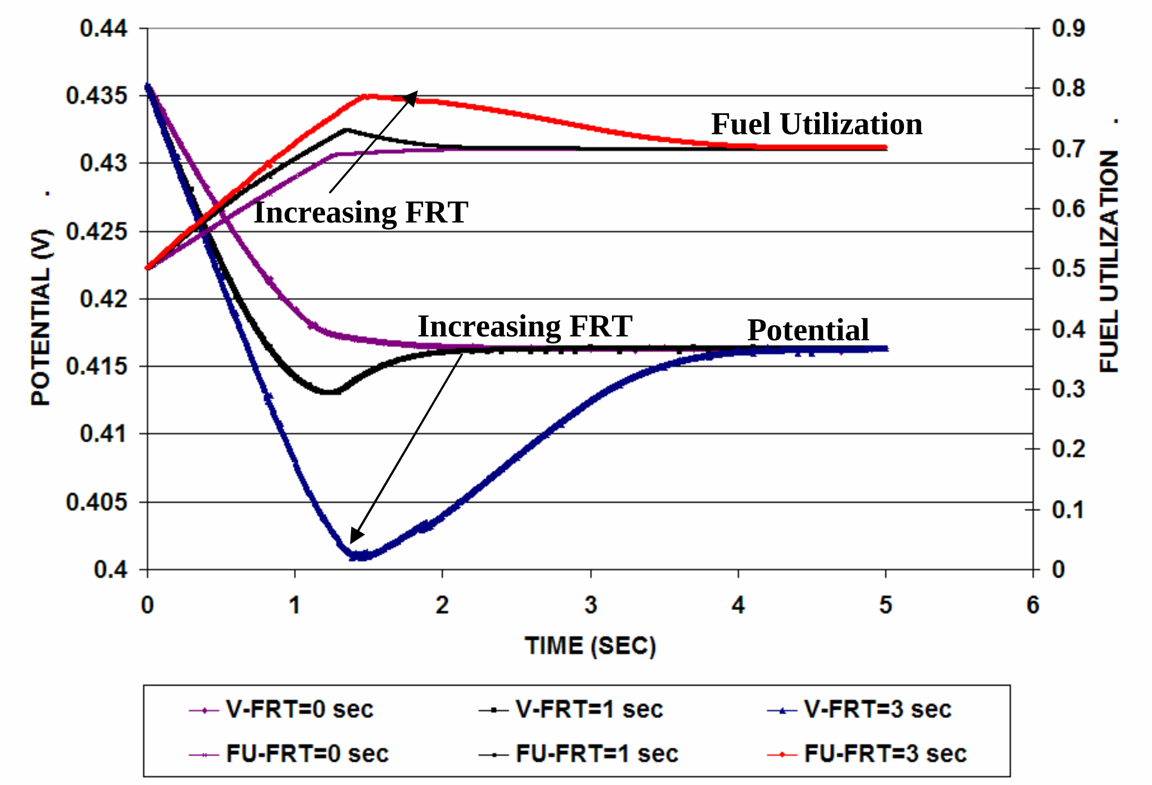

Figure 3.8. Electrical transient responses to bi-modal stimuli of a current density step change of 350 to 600 mA/cm^2 with fuel ramp rate times (FRT) of zero, one, and three seconds. (Note how increasing FRT results in a more pronounced overshoot and undershoot in the fuel utilization and voltage profiles, respectively.)

The significant observations of Figure 3.7 are the overshoot and undershoot responses of the fuel utilization and cell potential profiles, respectively. The fuel utilization overshoot response is representative of the larger relative reactant consumption rate caused by the “sharply” increased current demand in conjunction with delayed changes in reactants supply (especially fuel). The voltage undershoot is caused primarily by correspondingly magnified decreases in local Nernst potentials and limiting current densities along the cell. The latter effect of smaller limiting current densities exacerbates concentration polarization losses. As a result, the cell performance (i.e. cell potential) is degraded; henceforth, the cell potential profile displays an undershoot characteristic. The relatively exaggerated undershoot profile seen in the cell potential transient episode for the three second FRT clearly shows the loss in performance due to concentration polarization. The increase in current demand requires that the electrochemical reaction rates increase and, therefore, limitations occur due to smaller reactant availability. Extended transitional times for the fuel supply subsystem will therefore adversely impact the electrical performance. However, if the transitional times for the fuel supply subsystem is less than three seconds, then the undershoot trend in the cell potential response is less than 10% and is 5% for fuel ramp times less than one second.

Figure 3.7 shows that the electrical transient response due a step change (FRT=0) of a SOFC is on the order of seconds. However, the work of Achenbach [17] and others [18, 27] report a dynamic electrical response to a step change in load on the order of 100 seconds. As noted by the Qi et al. [27], the reason for the slow response is due to the slow temperature dynamics. The temperature transients arise due to the step change in load thereby causing a change in cell heat generation. The aforementioned authors considered temperature transients within their electrical transient model, whereas the electrical transient model does not include temperature dynamics; however, it captures the smaller time-scale non-thermal transient effects. Further discussion of the dynamic time scales of SOFCs will be given in the next chapter.

An enhanced electrical transient performance model has been presented. A novel rediscretization methodology was developed which facilitated the ability to simulate the dynamic response to bi-modal stimuli. The variable FRT was introduced to illustrate the impact that fuel supply rate transients have on cell performance. It was discovered that as

FRT increases, an overshoot and undershoot response was observed in the fuel utilization and cell potential profiles, respectively. Since the electrical transient model has been presented, complementary modeling efforts will be discussed in the next chapter.

CHAPTER 4

COMPLEMENTARY MODELING

4.1 Time Scale of Dynamic Modeling of SOFCs

As observed by Haynes [4], the thermal transients typically occur within of tens of minutes, whereas electrical and anodic mass transfer transients occur within seconds and fractions of seconds, respectively. Figure 4.1 shows the distinct time scales that impact the dynamic modeling of SOFCs.

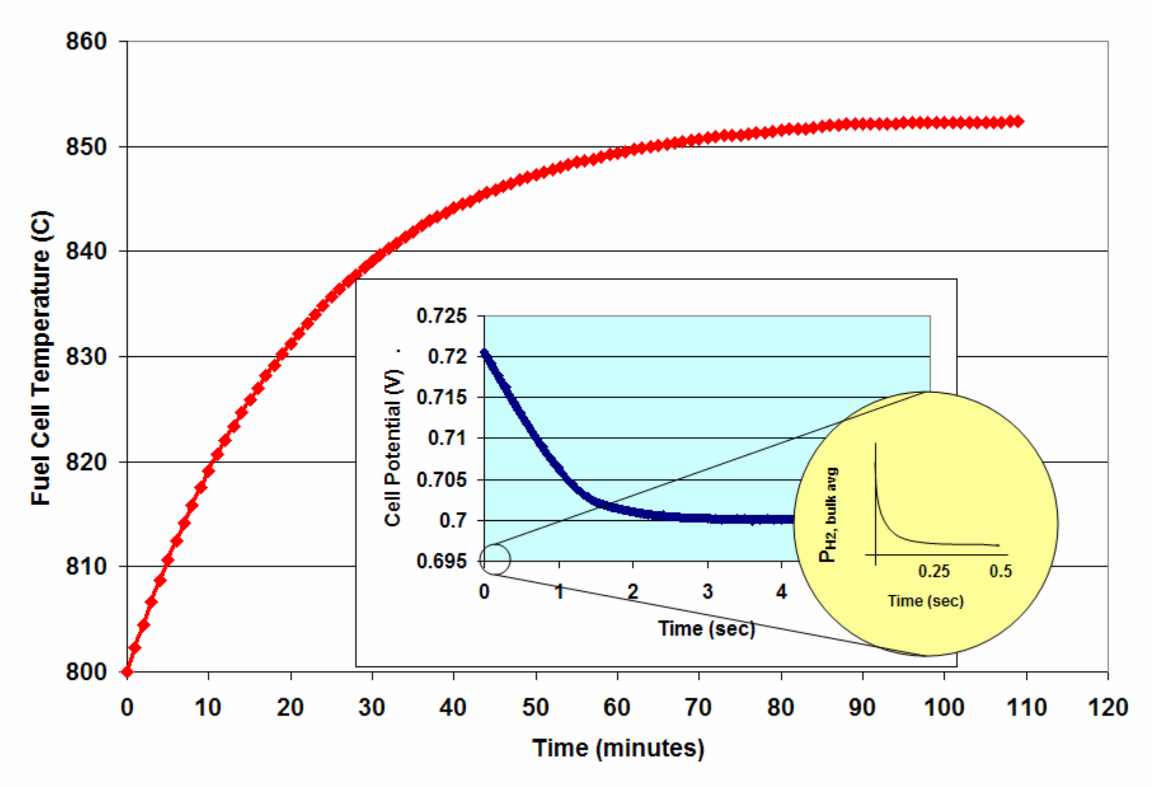

Figure 4.1. Diagram showing the three distinct dynamic time scales associated with SOFCs: thermal transients (on the order tens of minutes), electrical transients (on the order of seconds), and anodic mass transfer transients (on the order of fractions of seconds).

In the previous chapter, the electrical transients modeling presumed a quasi steady state anodic mass transfer scenario relative to the electrical transients. However, it has been postulated by Gemmen et al., [28] that there are relevant transient anodic mass transfer effects that occur. Therefore, there is a need to demonstrate the relevance of transient anodic mass transfer effects with respect to electrical transients. A time constant analysis was completed wherein the time constants associated with anodic mass transfer and electrical transients were determined and compared.

4.2 Time Constants Analysis

4.2.1 Methodology

The diffusion of hydrogen through a porous anode is shown in Figure 4.2 below. The modeling of anodic mass transfer transients presumed three important locations: the fuel stream, the bulk anode region, and the electrolyte/anode interface as depicted by the circle locations in Figure 4.2.

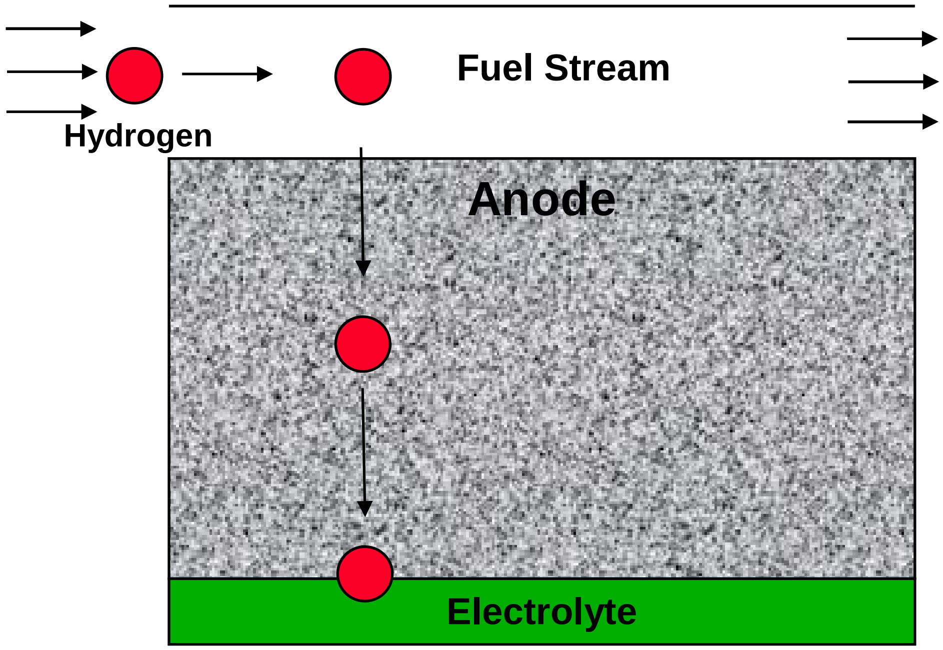

Figure 4.2. Hydrogen mass diffusion through the porous anode.

The aim of the time constant study was to ascertain the validity of presuming steady-state anodic mass transfer (i.e., negligibly small diffusional time scales) during an electrical transient episode. As introduced in Chapter 3, a fuel ramp time (FRT) of zero seconds was prescribed to simulate an instantaneous change in fuel flow rate. With FRT set to zero seconds, this will yield the smallest possible electrical time constant and therefore offer the best (i.e., most conservative) comparison case for the anodic mass transfer time constant. Additionally, this simplifies the initial comparison of anodic and electrical time constants, because there is no potential confounding effect associated with variable FRT.

As per the methodology used in developing an anodic mass transfer time constant, a lumped capacitance approach (i.e., a first order ordinary differential equation) regarding anodic partial pressure was taken wherein it was presumed that the net change in partial pressure is directly proportional to the step change in current demand. A related simplification of the approach was that a change in convective mass transfer from the fuel stream to the anode (due to changes in molar supply rates and/or anodic partial pressures) was neglected. By convention, the time constant for mass transfer is the time when there is approximately a 63% percent change in *average* partial pressure of hydrogen. The lumped capacitance approach for calculating the anodic mass transfer time constant motivated the development of an average anodic partial pressure of hydrogen. This is illustrated in Figure 4.3.

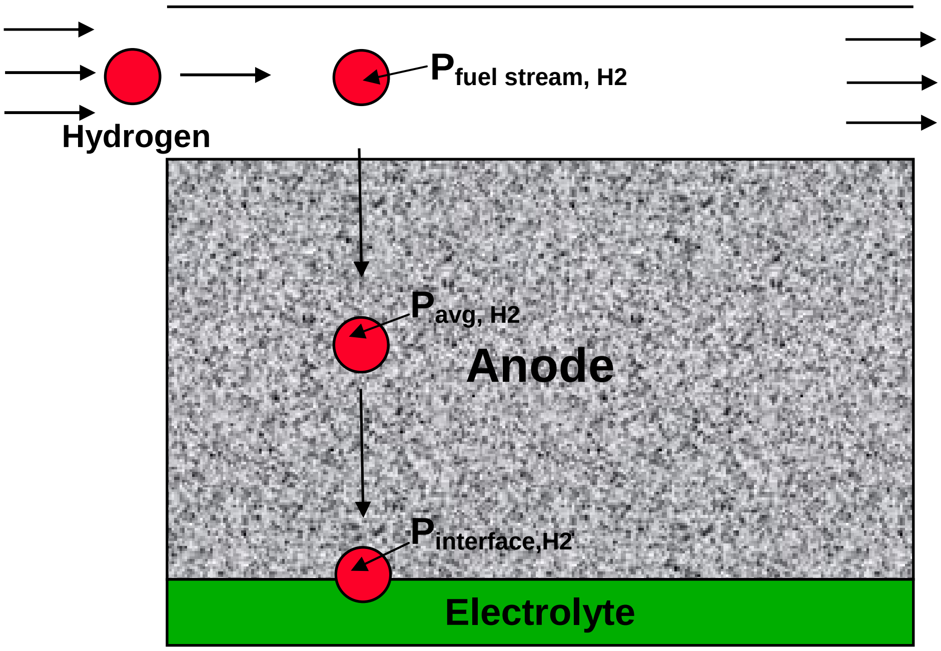

Figure 4.3. The lumped capacitance approach for developing a bulk average partial of hydrogen in the porous electrode.

The *slice* average partial pressure of hydrogen for this development is defined as the arithmetic mean of the fuel stream partial pressure and the partial pressure at the electrolyte/anode interfacial surface which is given in the following equation.

$$P_{avg,slice,H_2} = \frac{P_{\text{fuel stream,slice,H}_2} + P_{\text{interface,slice,H}_2}}{2} \tag{4.1}$$

For initial steady-state condition, the *(global)* average partial pressure is actually a "local current" weighted measure. This definition stems from the previously stated presumption that the net change in pressure is directly proportional to the change in current demand.

$$P_{avg,init,H_2} = \frac{\sum P_{avg,slice,H_2} i_{slice}}{i_{total}} \tag{4.2}$$

Knowing that the hydrogen in the porous electrode obeys the ideal gas law, the time rate of change of the average partial pressure of hydrogen may be described in this by the following ordinary differential equation:

$$\dot{P}_{avg,H_2} = \frac{\dot{n}_{change} R_u T}{\varepsilon V} \tag{4.3}$$

where R_u is the universal gas constant, T is the absolute temperate of the anode (presumed to be equal to the cell operating temperature), ε is the porosity of the anode, and V is the anode volume. The change in molar flow rate is constant and is directly proportional to the change in current as described by Faraday's law.

$$\dot{n}_{change} = \frac{\Delta i}{2F} \tag{4.4}$$

With the initial condition defined in Equation (4.2), an Eulerian approach was utilized in solving Equation (4.3) for the time at which there is a 63% change in pressure as described in the following equation.

$$P_{avg,H_2}(t+\Delta t) = P_{avg,H_2}(t) - \left|\dot{P}_{avg,H_2}\right|\Delta t \tag{4.5}$$

4.2.2 Time Constant Analysis Results and Discussion

For the initial case described in Table 4.1, the time constants associated with anodic mass transfer and electrical transients (with a FRT of zero) are given in Table 4.2.

Table 4.1. Initial conditions for the time constant simulations.

Parameter	Value	Units
NOS	6	---
Cell Temp	800°	C
ASR	0.665	Ω-cm^2
Initial Fuel Utilization	50	%
Initial Current Density	600	mA/cm^2

Table 4.2. Time constant results for the first case.

Increase in Load	$\tau_{\text{mass transfer}}$ (s)	$\tau_{\text{electrical}}$ (s)	Ratio
30 % (180 mA/cm^2)	0.128	0.392	3.06
40% (240 mA/cm^2)	0.096	0.504	5.25
50% (300 mA/cm^2)	0.080	0.704	8.80

The time constants associated with anodic mass transfer were smaller than that of the electrical *(*primarily *fuel stream effects)* time constants as anticipated. Additionally, the anodic mass transfer time constants decreased as the change in current demand increased, while the opposite was true for the electrical time constants. The anodic mass transfer time constant *decreases* with increasing change in current demand because the rate of change in reactant presence is directly proportional to the change in current demand as described in Faraday's law shown in Equation (4.5). Therefore, by the ideal gas law, the time rate of change of the partial pressure of hydrogen is directly proportional to the change in current, thus accounting for the trends observed for the anodic mass transfer time constant. The electrical time constant trends, however, can be associated primarily with changes in fuel stream composition. The consumption of hydrogen is directly proportional to current demand; hence, an increase in current demand results in the composition of the fuel stream (e.g., the molar concentrations of hydrogen) becoming transient. The larger instantaneous increases in fuel supply, however, which accompany larger increases in current demand (FRT is zero); buffer or dampen corresponding changes in stream composition and cell potential. Larger stimuli (i.e. current increase) then result in smaller relative rates of change with respect to cell potential.

It was hypothesized that initial current density does not change the time constants associated with anodic mass transfer and electrical transients. However, when the initial current density was reset from 600 mA/cm^2 to 350 mA/cm^2 (with other initial conditions remaining the same as detailed in Table 4.3), it was observed (ref. Table 4.4) that both associated time constants were *greater*.

Table 4.3. Second case initial conditions.

Parameter	Value	Units
NOS	6	---
Cell Temp	800°	C
ASR	0.665	Ω-cm^2
Initial Fuel Utilization	50	%
Initial Current Density	350	mA/cm^2

Table 4.4. Time constant results for the second case.

Increase in Load	$\tau_{\text{mass transfer}}$ (s)	$\tau_{\text{electrical}}$ (s)	Ratio
30 % (180 mA/cm^2)	0.24	0.772	3.22
40% (240 mA/cm^2)	0.18	0.808	4.48
50% (300 mA/cm^2)	0.144	1.04	7.22

For anodic mass transfer, the intensive property of note is initial hydrogen partial pressure, which *increases* as current demand decreases; thus, the time to reach a 63% change in the initial partial pressure of hydrogen is potentially greater for the smaller initial current density (i.e., larger initial hydrogen presence) cases. Table 4.5 illuminates this point. Additionally, regarding both anodic and electrical time constants, smaller initial current densities will result in smaller changes thereof; thus, the 350 mA/cm^2 scenario leads to smaller stimuli (i.e., current density changes) for a given percentage increase in current demand. The smaller stimuli will lead to longer response times and larger time constants.

Table 4.5. Hydrogen partial pressure values to illustrate the reason for time constant dependence on initial current demand for a 30% increase in load.

Initial Current Density (mA/cm^2)	P_{avg,int,H_2} (N/cm^2)	$\dot{P}_{avg,\text{int},H_2}$ (N/(s-cm^2))
600	11.2	37.0
350	12.2	21.6

As was previously stated, the intent of this study was to ascertain the operating conditions for which anodic mass transfer may not be treated as steady. Accordingly, an initial "time constants ratio" mapping has been done. More specifically, time constant ratios (i.e., $\tau_{\text{electrical}} : \tau_{\text{mass transfer}}$) have been established as a function of initial current demand and percent change in load. Such a mapping is shown in Figure 4.4.

There are two key observations in Figure 4.4. First, the time constant ratio increases with percentage increase in load current demand (i.e., in the 30%-50% range). This finding was expected due to the initial results shown in comparing the 350 mA/cm^2 and 600 mA/cm^2 cases. Secondly, minima occur between 400-450 mA/cm^2. The anodic mass transfer time constant decreases with current density as shown in Figure 4.5. Since the rate of change of the partial pressure of hydrogen, $\dot{P}_{avg,\text{int},H_2}$, is directly proportional to the change in current as shown in Equations 4.4 and 4.5, as well as the fact that larger initial currents result in smaller anodic hydrogen partial pressure, then it follows that larger initial current densities will yield smaller time constants (i.e, faster attainment of 63% change). Therefore, a decreasing monotonic trend is observed in the anodic mass transfer time constant profile. The minimum between 400-450 mA/cm^2 is therefore caused primarily by the minima that occur with the electrical time constant trend as shown in Figure 4.6.

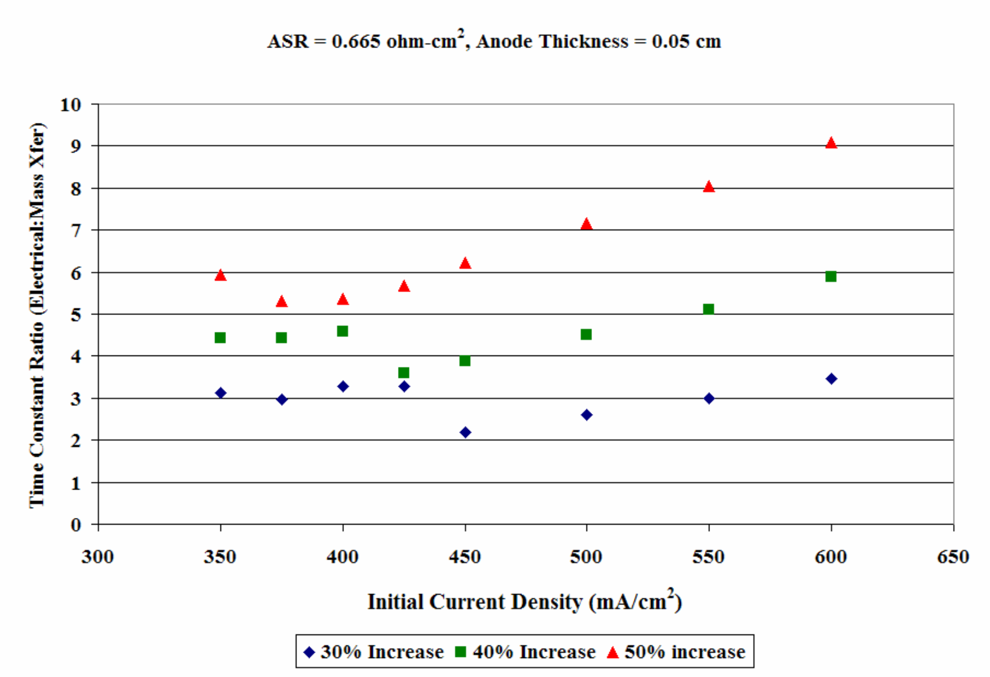

Figure 4.4. Time constant ratio (electrical: mass transfer) mapping showing dependence on initial current demand and percent load increase.

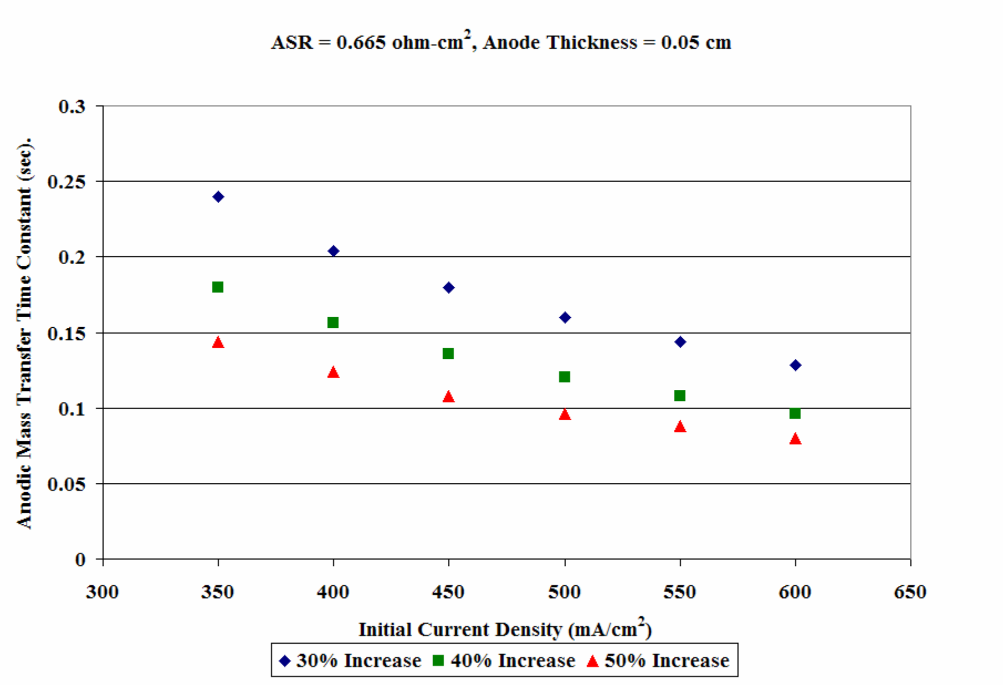

Figure 4.5. Anodic mass transfer time constant mapping showing dependence on initial current demand and percent load increase.

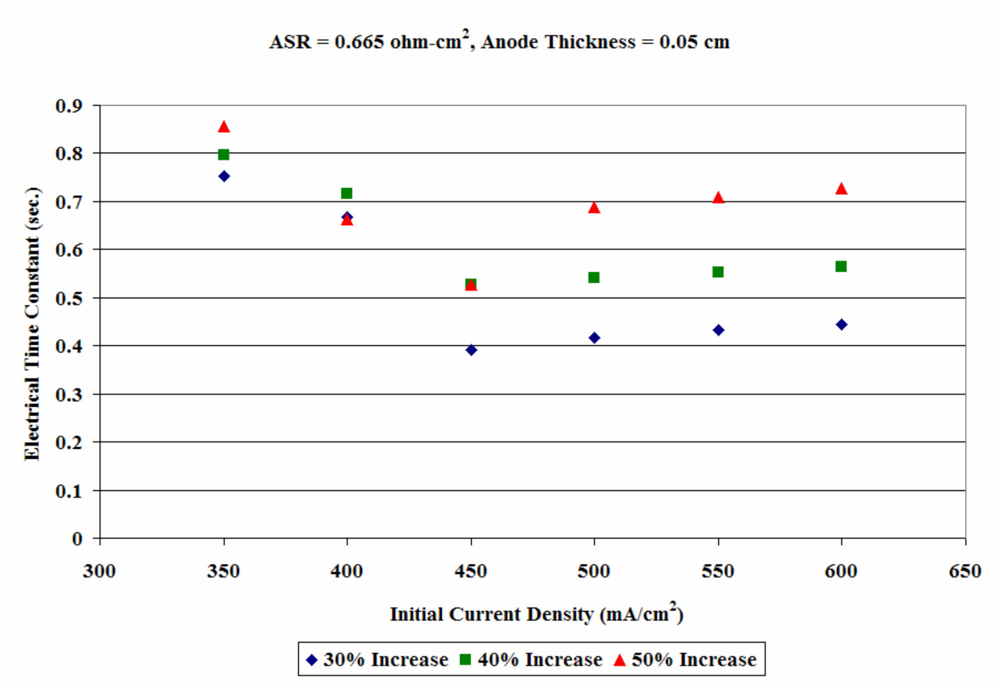

Figure 4.6. Electrical time constant mapping showing dependence on initial current demand and percent load increase.

It was initially hypothesized that a minima occurs between 400-450 mA/cm^2 because of a parameter of the SOFC and not a numerical singularity; and therefore one should see a shift in the location of the time constant ratio minima when design conditions change. To test this hypothesis, the ASR and anode thickness were decreased. Figure 4.7 shows the impact of decreasing ASR from 0.665 to 0.50 Ω-cm^2 on the time constant ratio mapping. As was hypothesized, the location of the minimum did shift. However, there are variable comparisons trends observed in Figure 4.7. Observe that the anodic mass transfer time constant is not impacted by ASR because of its dependence on change in current and the mass capacitance of the anode as illustrated in Figure 4.8. Therefore, the variability is attributed to the electrical time constant profile shown in Figure 4.9.

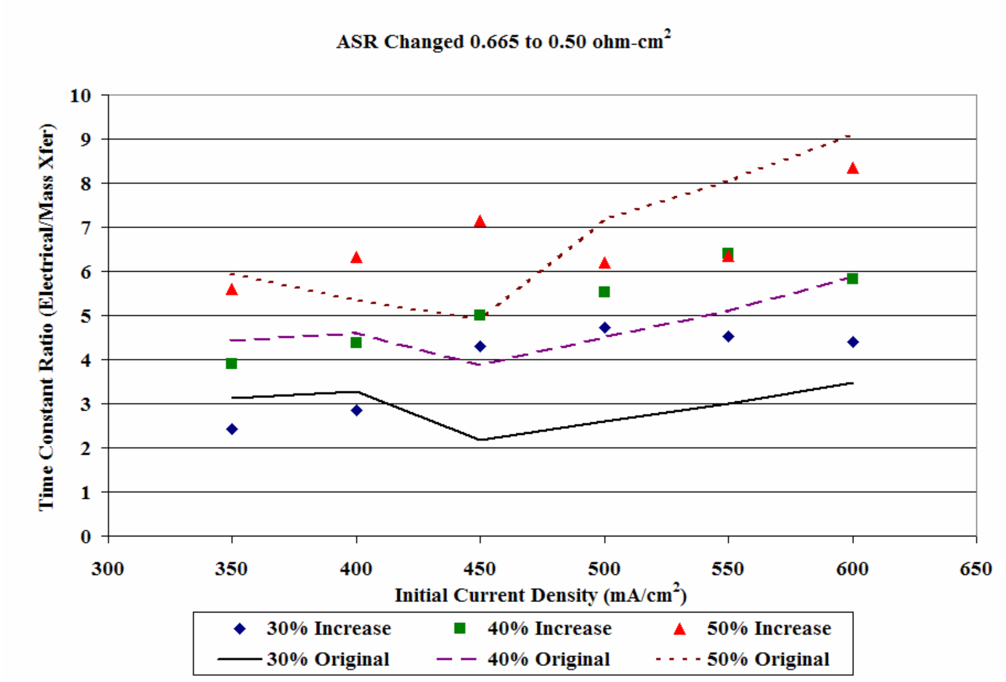

Figure 4.7. Time constant ratio (electrical: mass transfer) mapping showing dependence on initial current demand and percent load increase with ASR changed to 0.50 Ω-cm^2.

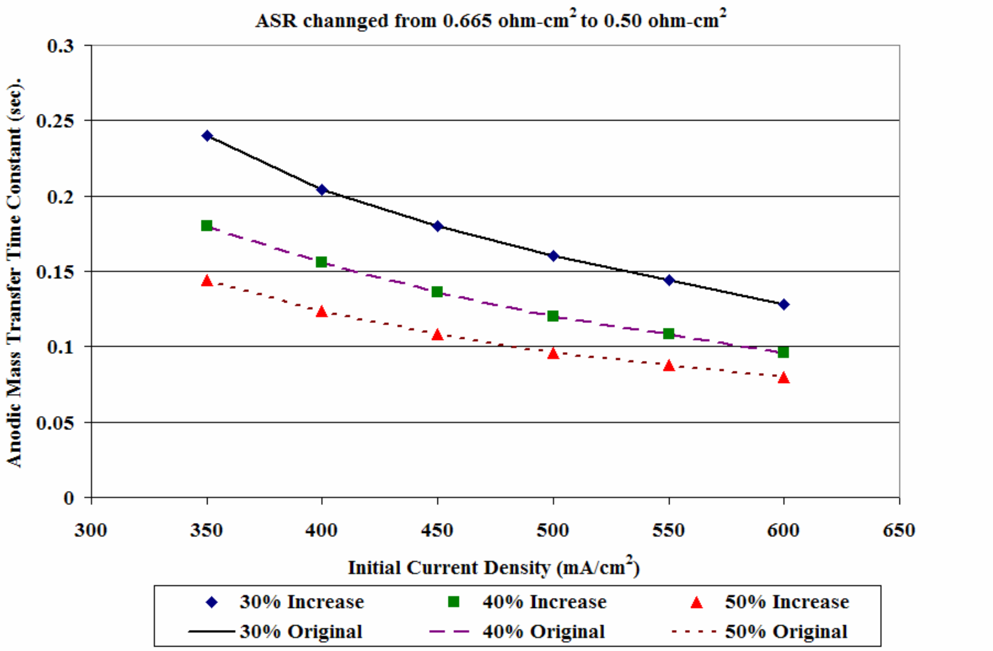

Figure 4.8. Anodic mass transfer time constant mapping showing dependence on initial current demand and percent load increase with ASR changed to 0.50 Ω-cm^2.

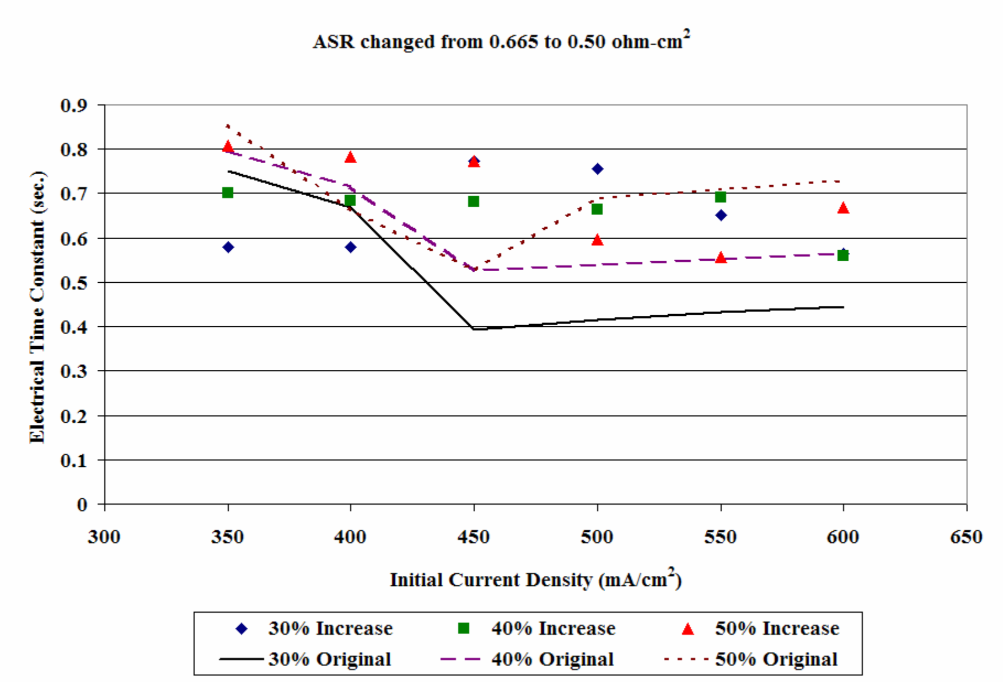

Figure 4.9. Electrical time constant mapping showing dependence on initial current demand and percent load increase with ASR changed to 0.50 Ω-cm^2.

The significant variability in electrical time constant trends and profiles is presently attributed to a dynamic mixture of contributions from fuel stream transients and nonlinear polarization sensitivities. Again, electrical time constant functionality is the primary "driver" of overall time constants ratio sensitivity.

Since the SOFC material parameter ASR impacted the time constant ratio trends, it was expected that a geometric parameter such as anode thickness would also affect the time constants ratio trends. Figure 4.10 shows the result of decreasing the anode thickness from 0.05 cm to 0.04 cm on the time constant ratio mapping. In all three scenarios, the time constant ratio profiles changed relative to the baseline cases. In contrast to the baseline cases, the profiles increased to intermediate maxima. Furthermore, each scenario differed in terms of which current density did the time constant ratio was a minimum reached. Further explanation for the reasoning for the observed trends can be elucidated from the electrical time constant and anodic mass transfer time constant mappings as shown in Figure 4.11 and Figure 4.12, respectively.

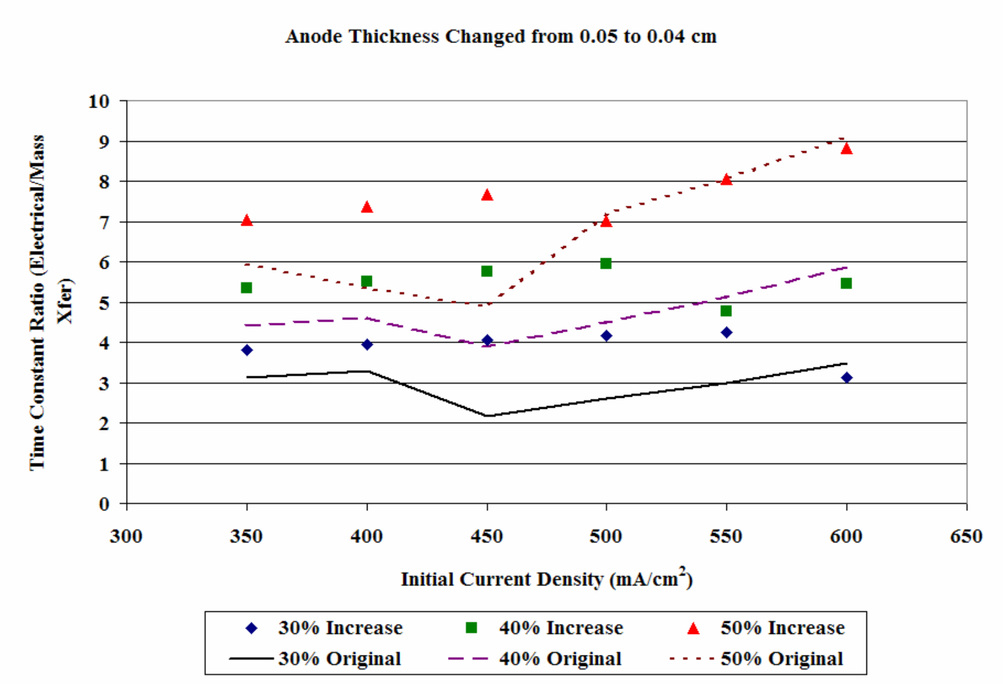

Figure 4.10. Time constant ratio (electrical: mass transfer) mapping showing dependence on initial current demand and percent load increase when anode thickness is decreased to 0.04 cm.

Although all the electrical time constants decreased until the minimum current density was reached, the time constant ratio increased over the same range of current densities as illustrated in Figure 4.11 and Figure 4.10, respectively. Figure 4.12 shows the cause of this trend. Figure 4.11 shows the mass transfer time constant decreasing at a greater rate (and with smaller in values) than that of the electrical time constant.

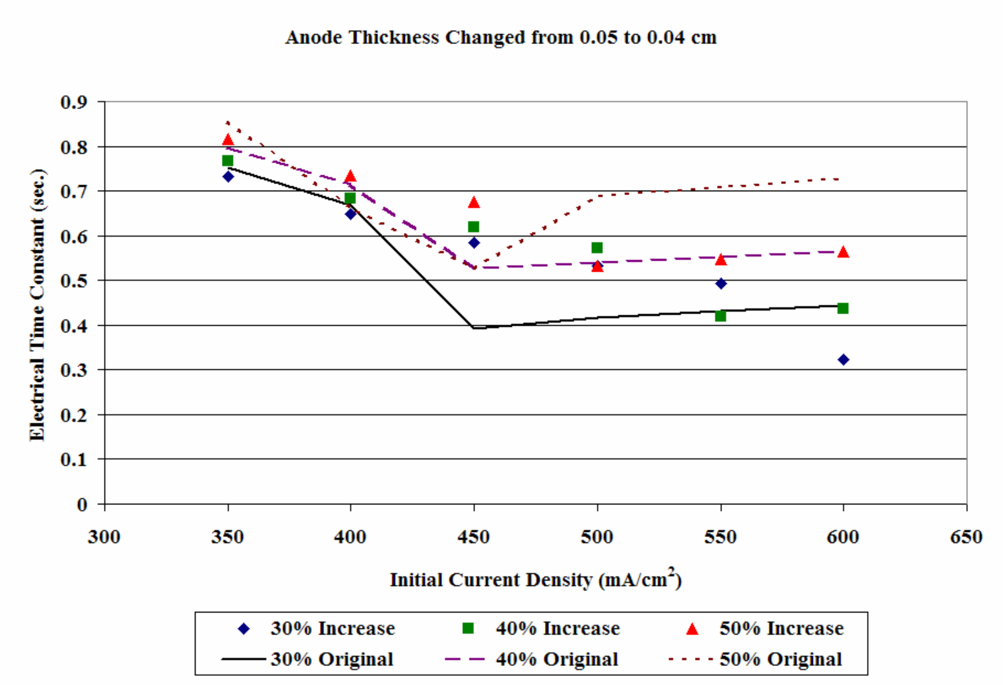

Figure 4.11. Electrical time constant mapping showing dependence on initial current demand and percent load increase when the anode thickness is decreased to 0.04 cm.

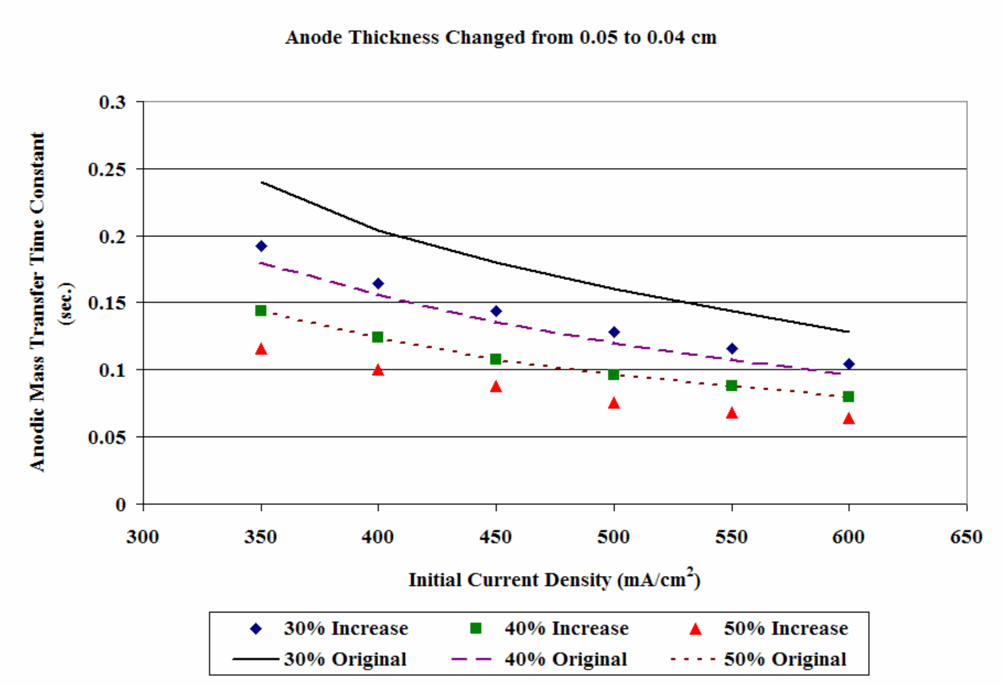

Figure 4.12. Anodic mass transfer time constant mapping showing dependence on initial current demand and percent load increase when the anode thickness is decreased.

4.2.3 Time Constant Analysis as FRT→ ∞

It was initially hypothesized that as FRT approaches infinity, then the time constant ratio mapping would change compared to when FRT is zero. Prescribing FRT to approach infinity describes a scenario when the fuel supply rate takes an infinite amount of time to attain the final steady state fuel supply rate (i.e. approximately fixed fuel supply rate). Recall that prescribing FRT is zero simulates a scenario when the fuel supply rate instantly changes to the final fuel supply rate. However, when Figure 4.13, which is the resulting time constant mapping for FRT approaching infinity, is compared to Figure 4.5, the results are identical. Since the anodic mass transfer methodology is primarily a function of change in current, then the expected deviation would be due to the electrical time constant. The electrical time constant mapping is shown in Figure 4.14 and is discussed below.

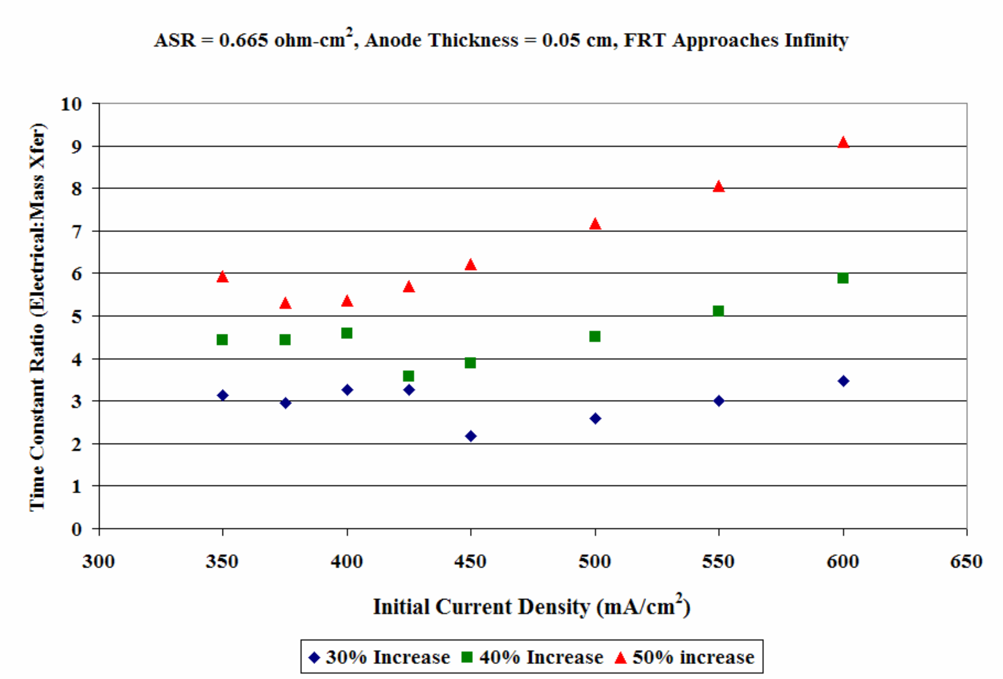

Figure 4.13. Time constant ratio (electrical: mass transfer) mapping showing dependence on initial current demand and percent load increase.

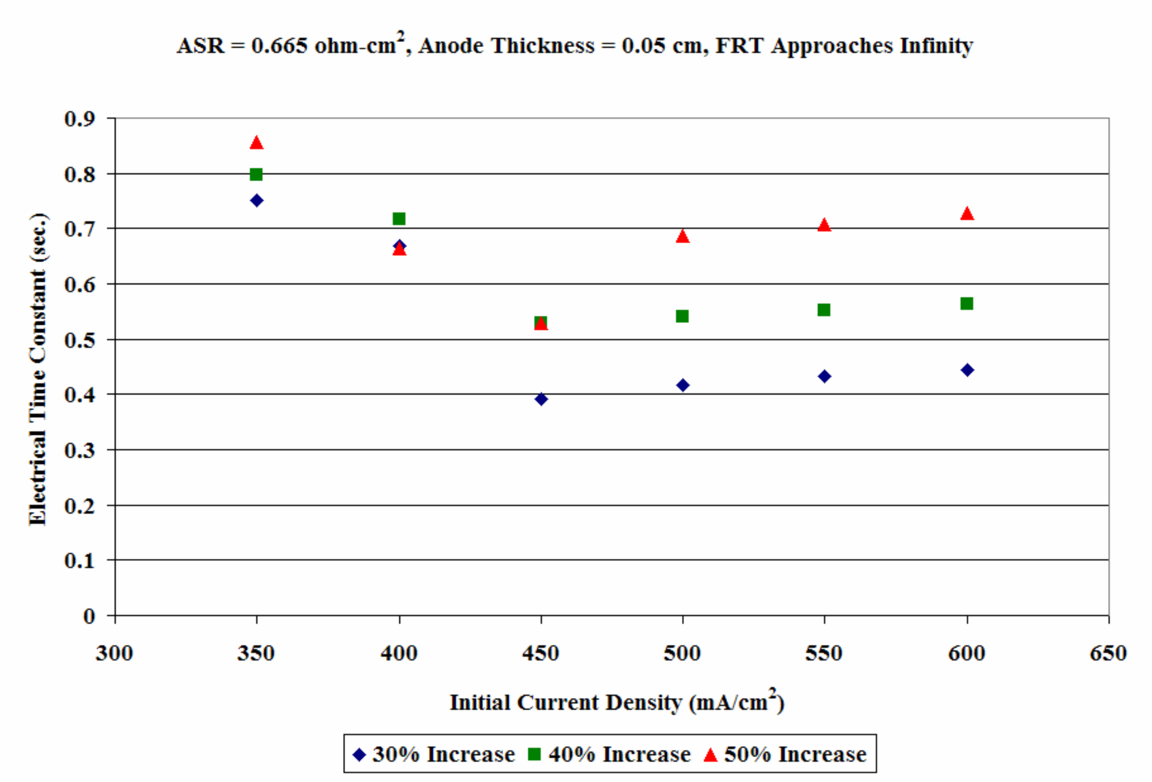

Figure 4.14. Time constant ratio (electrical: mass transfer) mapping showing dependence on initial current demand and percent load increase.

In comparing the electrical time constant mapping shown in Figure 4.14 (FRT→∞) with Figure 4.6 (FRT = 0), the mappings are again identical. Therefore, although the fuel supply rate transitions are vastly different (i.e., a step change variation in fuel supply rate versus effectively none at all), the electrical time constants are identical given a prescribed change in current demand and duration of the simulation. As was shown in Chapter 3, the electrical time constant is influenced by both electrical and fluidic stimuli (i.e. bi-modal stimuli). The extreme FRT cases simulate a scenario wherein the fuel supply rates are essentially set after “t=0+”, which is obvious for the case when FRT is zero. When FRT approaches infinity, the fuel supply rate is changing at infinitesimally small increments; hence, the fuel supply rate may be presumed static.

The effect is then that the relative propagation of the fuel stream transient effects, which dominate cell response, will be the same for both cases.

4.2.4 Conclusions of Time Constants Analysis

A time constant ratio of ten (representative of an order of magnitude difference in time constants) is herein presumed sufficient to approximate quasi-steady state anodic mass transfer. In light of the results, some of which are significantly less than 10, it is important to cautiously impose the key simplification of quasi-steady state anodic mass transfer in electrical transients analysis. Therefore, it is emphasized that the mapping of time constants ratios is a conservative tool for diagnosing the need for including more rigorous anodic mass transfer within dynamic calculations. Due to the mapping's (Figures 4.4, 4.7, 4.10, and 4.13) conservative nature and findings, it is concluded that anodic mass transfer transients can be significant relative to electrical transients.

In addition, it was shown that initial current density, percent change in current, ASR, and anode thickness impact the electrical time constants. Electrochemical property and geometric values such as ASR and anode thickness, respectively, impact time constant values and hence the relevance of considering mass transfer dynamics. Lastly, both extreme FRT cases produced identical time constant ratio mappings due to the static (or nearly static) fuel supply rate condition in both scenarios after t=0+.

4.3 Electrolysis Modeling

4.3.1 Motivation and Problem Description

Shown in Figure 4.15, during planned (e.g., shutdown) or unplanned (e.g., load trip) reduction in load, a sharp decrease in current demand can lead to downstream electrolysis where the cell electrolytically produces hydrogen. Although the cell would eventually equilibrate to normal, fully galvanic operation this poses potential performance/reliability dangers as reported by Gemmen and Johnson [29-31], and Hawkes [32]. Since cell potential is a nearly uniform boundary condition, there exists a threshold voltage, which equals the end-of-cell Nernst potential that is a theoretical maximum potential for normal operation of the cell.

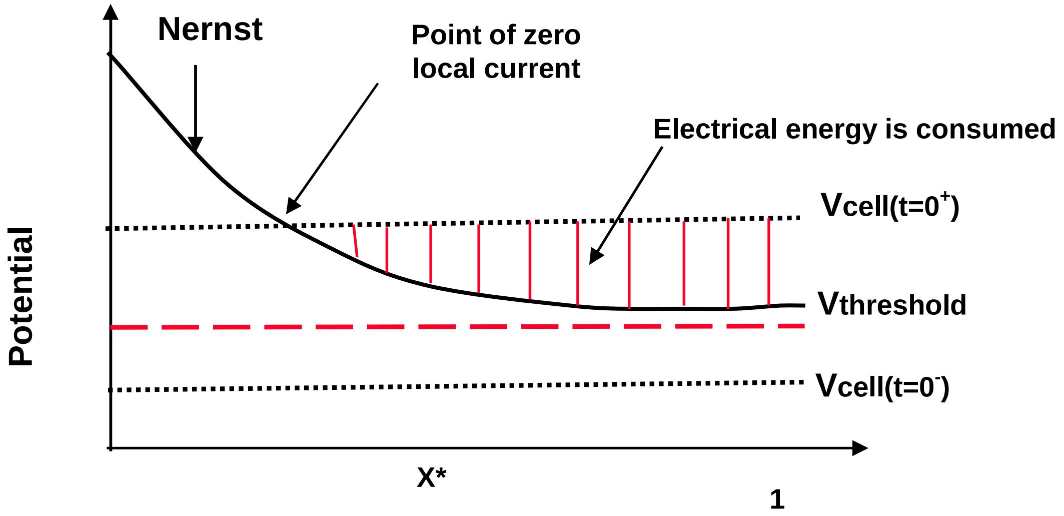

Figure 4.15. Diagram illustrating downstream electrolysis due to planned or unplanned steep decreases in load.

Steep decreases in current demand, given a slower decrease in fuel supply rate, can lead to a sufficient gain in cell potential such that the threshold voltage is surpassed and a “crossing” of the Nernst potential profile occurs as detailed in Figure 4.15. The point of “zero current” is where the cell potential equals the local Nernst potential. This is the point of demarcation between galvanic and electrolytic cell operation, and is partially a function of the initial fuel utilization and change in current demand.

4.3.2 Electrolysis Simulation Methodology

The two primary objectives in the electrolysis simulations were to ascertain the operating conditions and stimuli that would promote the onset of electrolysis, as well as the axial location of such initiations along the cell. Accordingly, initial fuel utilization and change (i.e., decrease) in current demand were varied between 50-85% and 225-450 mA/cm^2, respectively. All simulations were ended when downstream electrolysis occurred (i.e. exceeding of local Nernst potential).

4.3.3 Sample Results and Discussion of Electrolysis Modeling

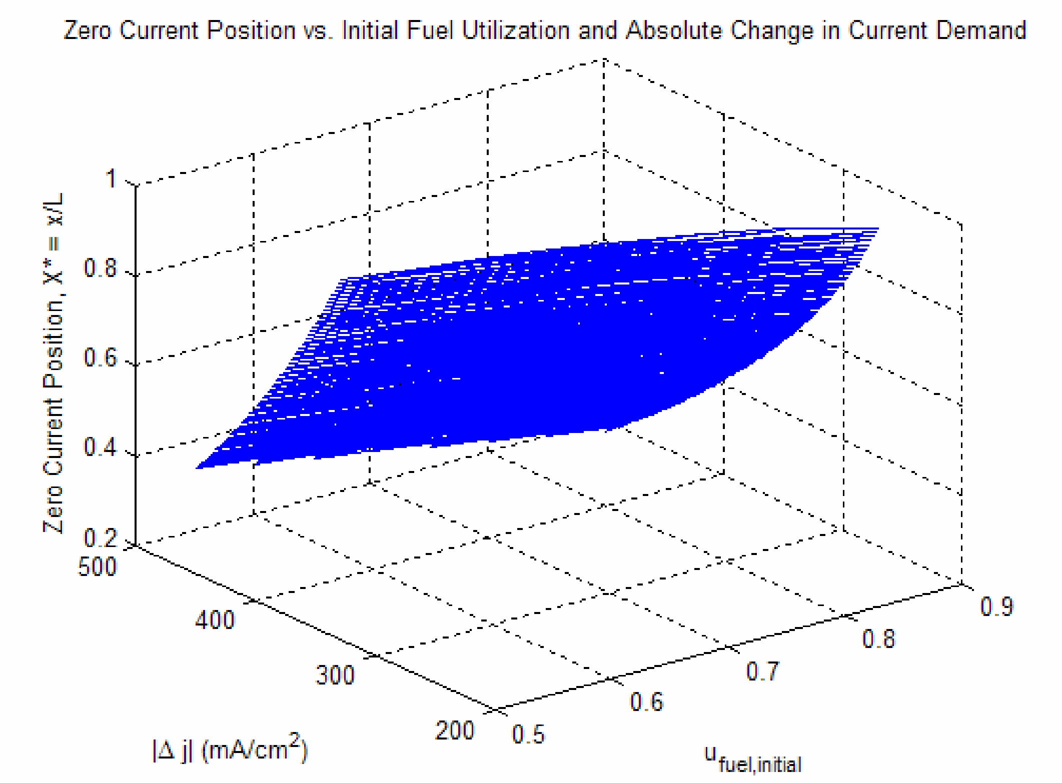

Figure 4.16. Zero current position profile as a function of initial fuel utilization and decrease in current demand.

Figure 4.16 shows the zero current position as a function of the current density reduction and initial fuel utilization, spanning between 225-450 mA/cm^2 and 50-85%, respectively. Figure 4.17 depicts that at high fuel utilizations the required decrease in current demand (to cause downstream electrolysis) is less than that at lower fuel utilizations. This is primarily due to lower end-of-cell Nernst potentials at higher fuel utilizations.

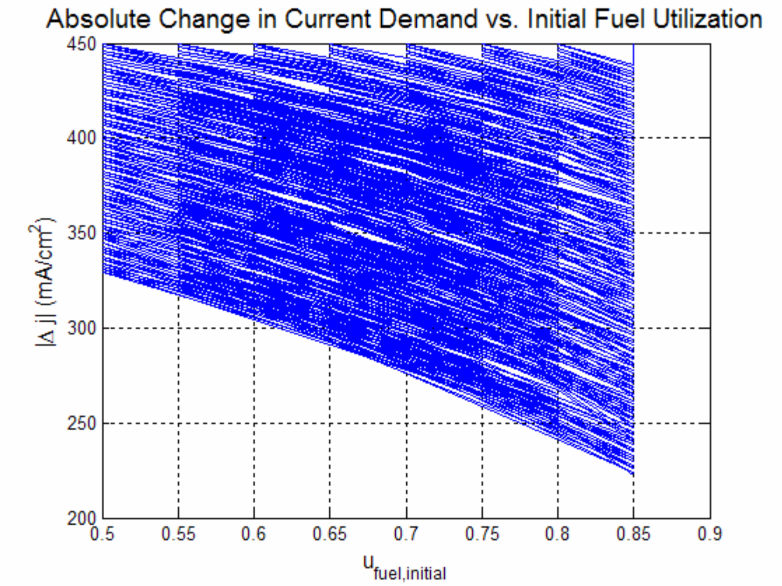

Figure 4.17. 2-D projection of electrolysis occurrence (shaded region) as a function of decrease in current demand and initial fuel utilization. Note that at higher fuel utilizations smaller decreases in current demand are sufficient to cause electrolysis.

Figure 4.18 shows the zero current point profile, this time as a function of voltage gain and initial fuel utilization. Again the initial current density is 600 mA/cm^2, and the domain of current density decreases are between 225 mA/cm^2 and 450 mA/cm^2. A larger range of voltage gains as shown in Figure 4.19 were observed at higher fuel utilizations, due to increased sensitivity of cell potential to changes in current demand.

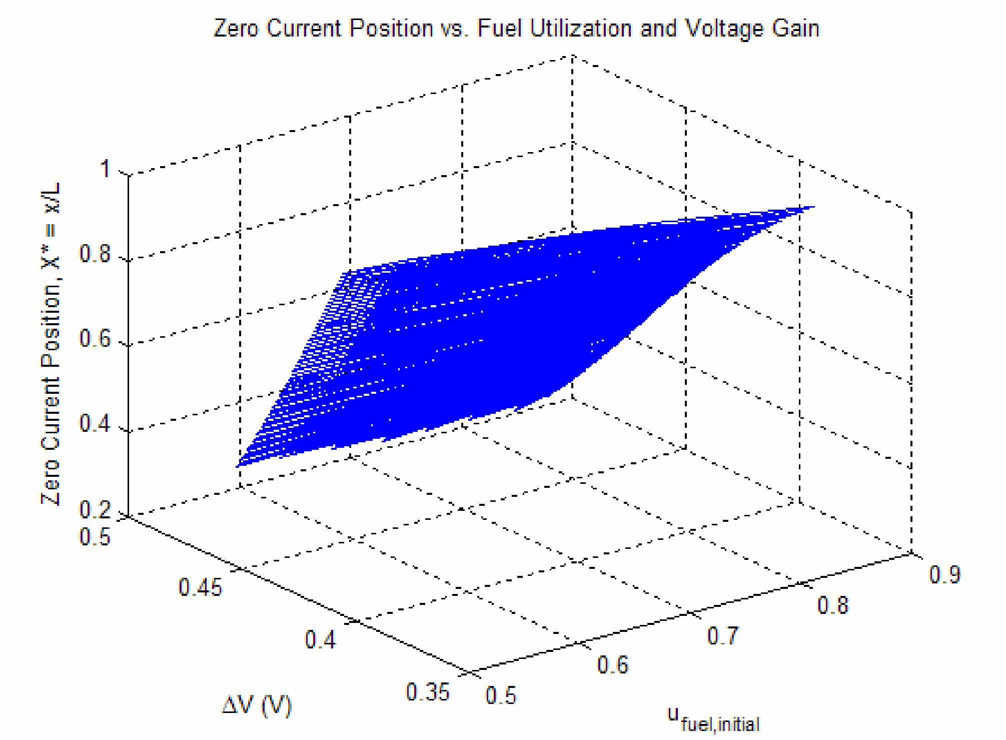

Figure 4.18. Zero current position profile as a function of fuel utilization and the resulting voltage gain.

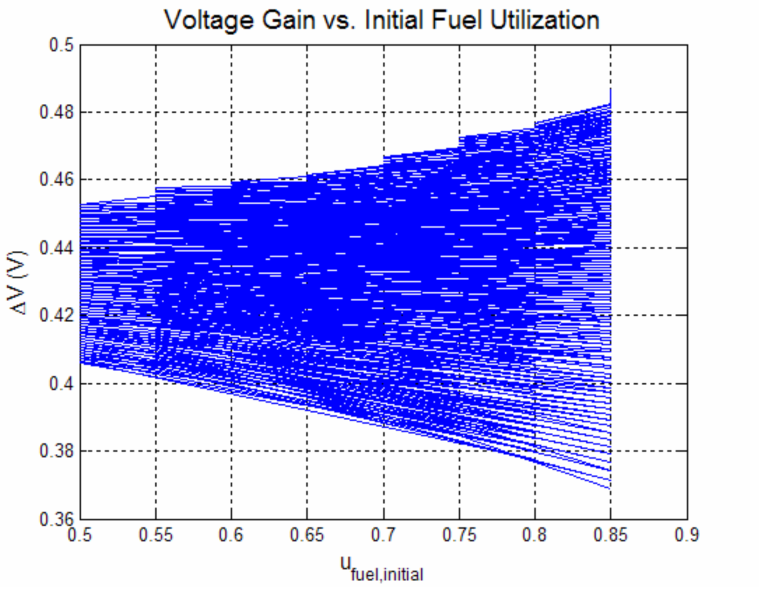

Figure 4.19. A projection of voltage gain vs. initial fuel utilization from the zero current position profile.

Figures 4.20 and 4.21 show the impact of fuel utilization on hydrogen partial pressure profiles and corresponding Nernst potential profiles, respectively. The significantly greater decrease in downstream Nernst potentials as a function of fuel utilization results in lower thresholds for electrolysis to occur. Given the present domain of scenarios, the lower threshold effect is dominant such that electrolysis was a likely event at higher fuel utilizations.

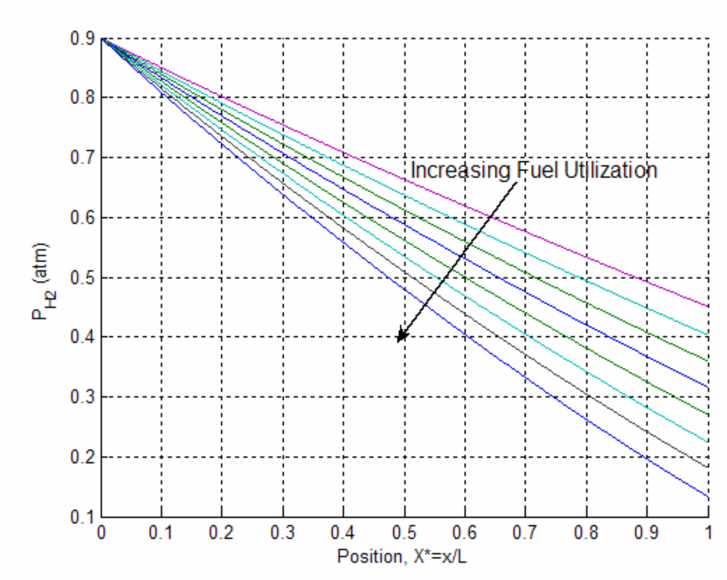

Figure 4.20. Graphic showing the impact of fuel utilization (i.e. in the range of 50-85%) on the partial pressure of hydrogen profile.

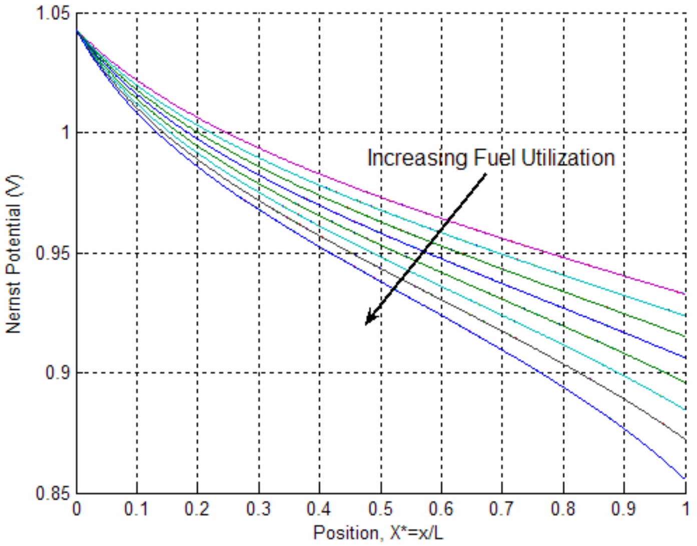

Figure 4.21. Graphic showing the impact of fuel utilization (i.e. in the range of 50-85%) on the Nernst potential profile. (Note how the Nernst potential profile decreases more significantly with increasing fuel utilization.)

4.3.4 Conclusions of the Electrolysis Simulations

It has been shown that fuel utilization and magnitude of the decrease in current demand determine when and where electrolysis will occur downstream (i.e., the point of zero current). A key observation is that at higher fuel utilizations there is a lower threshold for electrolysis to occur due to the significantly greater decrease in Nernst potentials relative to lower initial fuel utilizations. Correspondingly, steep changes in current demand combined with high initial fuel utilization values are conditions that promote electrolysis along the cell.

CHAPTER 5

ELECTROCHEMICAL LIGHT OFF SIMULATION

5.1 Problem Description

Given a cold start (i.e., at room temperature), the SOFC stack needs to be heated to a desired operating temperature, which is nominally 800°C for a planar SOFC stack. However, the electrochemical reactions that occur within SOFCs require a minimum temperature of approximately 650°C. During latter-stage “heat up” of the SOFC stack to a desired operating temperature, heat may strategically be generated from these electrochemical reactions as conveyed in Figure 5.1.

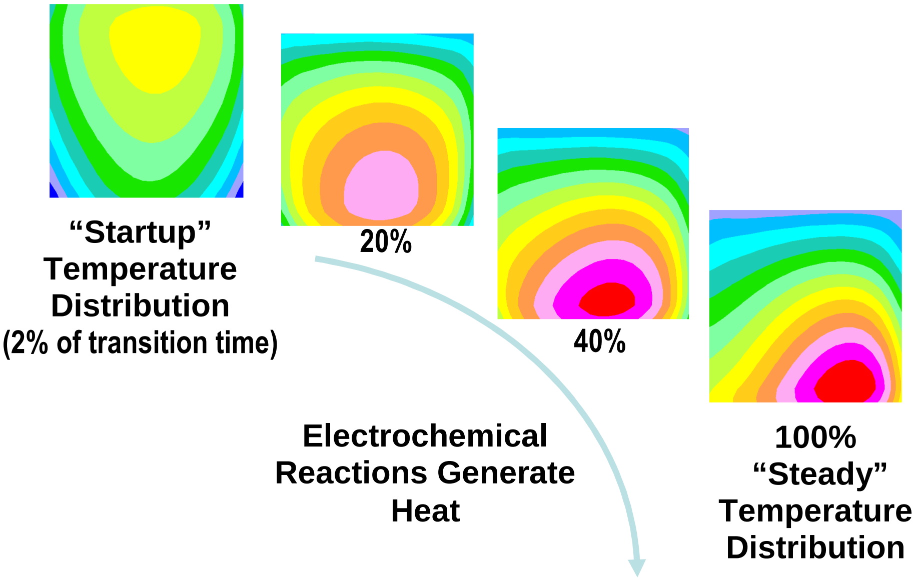
“Startup” Temperature Distribution (2% of transition time)
20%
40%
Electrochemical Reactions Generate Heat
100% “Steady” Temperature Distribution

Figure 5.1. Graphic illustrating the electrochemical light off phenomenon. [Courtesy of Pacific Northwest Laboratory.]

Due primarily to excessively large internal ohmic resistances, significant electrochemistry (and hence by-product heat) does not viably occur until a threshold temperature is reached (e.g., in the range of 550-650°C for conventional SOFCs). From such a threshold point, the temperature rise in the stack causes an acceleration of the electrochemical reactions (hence current) given a potentiostatic condition (i.e., prescribed cell potential). This occurs because of the significant reduction in electrochemical loss parameters such as electrolyte resistance at higher temperatures, and it symbiotically engenders more by-product (primarily Joule) heating. The interplay of the increasing heat generation and electrochemistry/current is herein termed “light off”, and a model has been developed to begin characterizing this important phenomenon.

As mentioned in the literature review, to date, there have been few, if any, studies that considered electrochemical operating conditions such as cell potential and current density as "dynamic controls" in managing light off transients. An investigation regarding the impact of electrochemical conditions on light off thermal transients has thus begun. The ultimate intent is to investigate the plausibility of using such electrical and electrochemical dynamic controls as a partial means of optimizing rapid, yet safe, thermal ramps for effective SOFC start-up.

5.2 Model Description

The present lumped capacitance model described in Equation 5.1 is used to simulate the thermal transients of the cell that occur during electrochemical light off.

$$C_{cell} \frac{dT_{cell}}{dt} = Q_{gen} - Q_{conv} \tag{5.1}$$

where T_{cell}, C_{cell}, Q_{gen}, and Q_{conv} are the unit cell temperature, heat capacitance, heat generation, and the convective heat transfer from the cell to the reactants streams (primarily air), respectively. Lumped capacitance is invoked for a few reasons. Given the present pilot study, a simplified transient approach is considered an appropriate lead into continuing studies wherein temperature gradients are resolved. Additionally, most

SOFCs are in fact intended for operation with minimal spatial temperature variation from a reliability standpoint (i.e., temperature uniformity is promoted to minimize thermally induced stresses which can cause component cracking and delamination when excessive). Finally, a key phenomenon near typical SOFC operating temperatures is that of *in situ* radiation which is expected to significantly reduce temperature gradients along the cell.

The heat capacitance is dominated by the stainless steel interconnect (i.e. due to its much larger mass fraction); while the dominant "heat sink" effect is that of the air flow. A quasi steady-state electrochemistry assumption is used, since thermal time constants are much larger than electrochemical ones. Additionally, the model assumes a static reactants supply conditions, and a co-flow unit SOFC arrangement. Furthermore, it is presumed that the initial fuel cell temperature, with respect to light off, is equal to the inlet air temperature (herein a representative parameter value of 650°C) due to the use of hot air to heat the stack before electrochemistry begins. Finally, temperature dependent properties such as heat capacitance and area specific resistance (ASR) are included in the modeling effort. The heat capacitance is calculated using a mass average (see Appendix for a more detailed calculation) of the relevant property values reported in the work of Gemmen et al. [29]. The limited access to ASR data prompted the use of the values provided by Kim et al. [25], which were tabulated for a temperature range of 650-800°C. It should be noted that conventional full cell and *stack* ASR values may be an order of magnitude higher than these button *cell* values; but the trends reported are expected to be the same. Therefore, the ASR datum from [25] was multiplied by a factor of 10 to obtain stack level estimates of ASR.

The simulation begins by first establishing the final steady state reactants supply conditions using the steady state electrochemistry model of [3]. The reactants flow rates are subsequently held constant during the entire transient simulation. The light off stimulus is the step change of the SOFC unit cell from open circuit voltage to a prescribed steady state voltage. A new cell temperature is calculated for each iteration between the thermal and electrochemical sections of the algorithm, which is depicted in Figure 5.2.

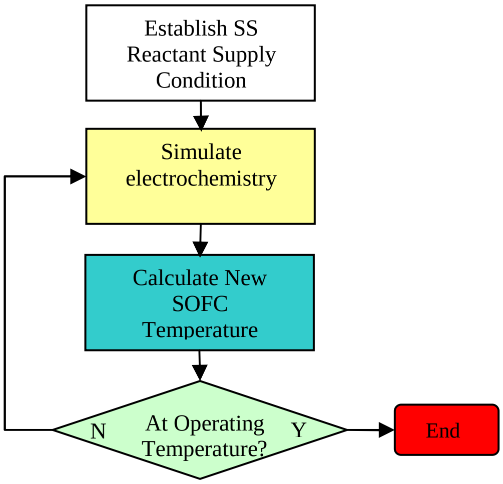
Establish SS Reactant Supply Condition
Simulate electrochemistry
Calculate New SOFC Temperature
N
At Operating Temperature?
Y
End

Figure 5.2. Flowchart/logic of computational approach of the electrochemical light off simulation.

5.3 Sample Results and Discussion

Table 5.1. Three electrochemical scenarios considered for the electrochemical light off simulations.

Cell Potential (V)	NOS (Air)
0.50	10.75
0.65	8.75
0.75	7.25

The three sets of operating conditions shown in Table 5.1 were simulated to study the effect of operating voltage on electrochemical light off. In this study, cell potential was used as the dynamic stimulus; the prescribed fuel utilization parameter 85% in all cases. The airflow rate was fixed at the final steady state value based upon the prescribed inlet air temperature condition (650°C) and the final steady state heat generation. With the airflow rate established, the "number of stoichs" or NOS (i.e. fuel based inverse equivalence ratio) of the air stream was calculated. The SOFC unit cell data and property values used in the simulation are given in Table 5.2.

Table 5.2. SOFC unit cell data and property values.

Parameter	Unit	Value(s)
Anode thickness	cm	0.05
Anode density	kg/m^3	4200
Anode specific heat	J/kg-K	640
Cathode thickness	cm	0.0075
Cathode density	kg/m^3	3300
Cathode specific heat	J/kg-K	570
Electrolyte thickness	cm	0.0015
Electrolyte density	kg/m^3	5100
Electrolyte specific heat	J/kg-K	600
Interconnect thickness	cm	0.5
Interconnect density	kg/m^3	8055
Interconnect specific heat	J/kg-K	602-623 [33]
Area Specific Resistance (ASR)	Ω-cm^2	0.178-0.068
Cell length	cm	10
Cell width	cm	0.5
Gas channel width	cm	0.25
Gas channel height	cm	0.25

As shown in Figures 5.3-5.4, smaller cell potentials caused the cell to reach steady state temperatures more rapidly. The primary reason for such is that lower cell potentials result in larger current generation. Larger current results in larger by-product heat via the stoichiometric relationship between current, reactants consumption (i.e., Faraday's Law) and corresponding thermal energy generation. This promotes faster temperature rise. Furthermore, the percent of the by-product heat absorbed by the cell decreases with time. This is a result of the increasing heat sink effect of the air flowing through the cell, as cell temperature rises. More specifically, the convective heat transfer from the cell to the air stream gradually becomes dominant in time; until the cell becomes completely heat rejecting.

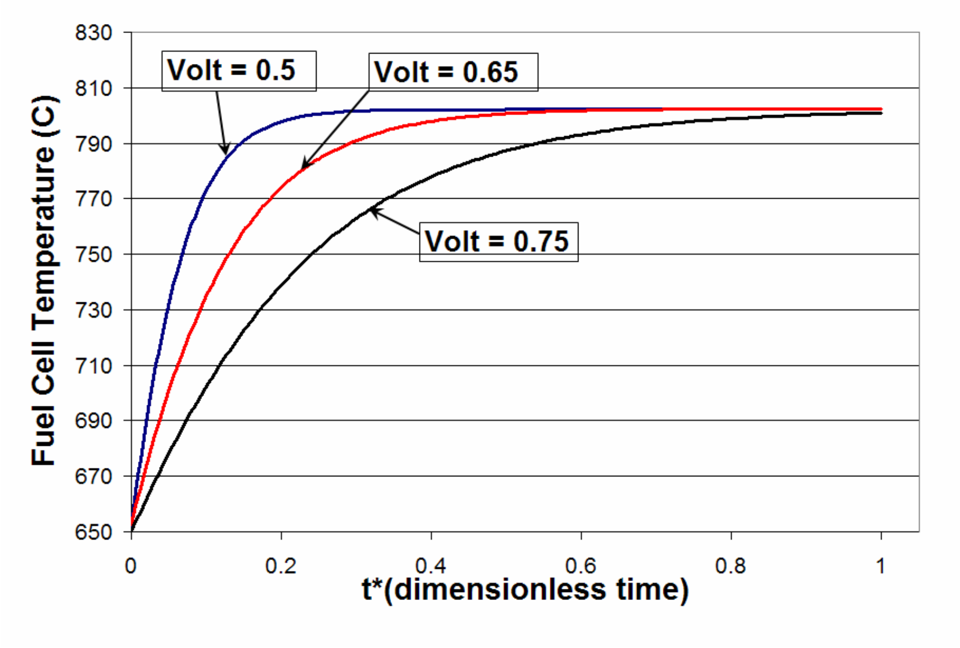

Figure 5.3. SOFC temperature response during electrochemical light off. (Note t*=t/T where T is 83.5 minutes.)

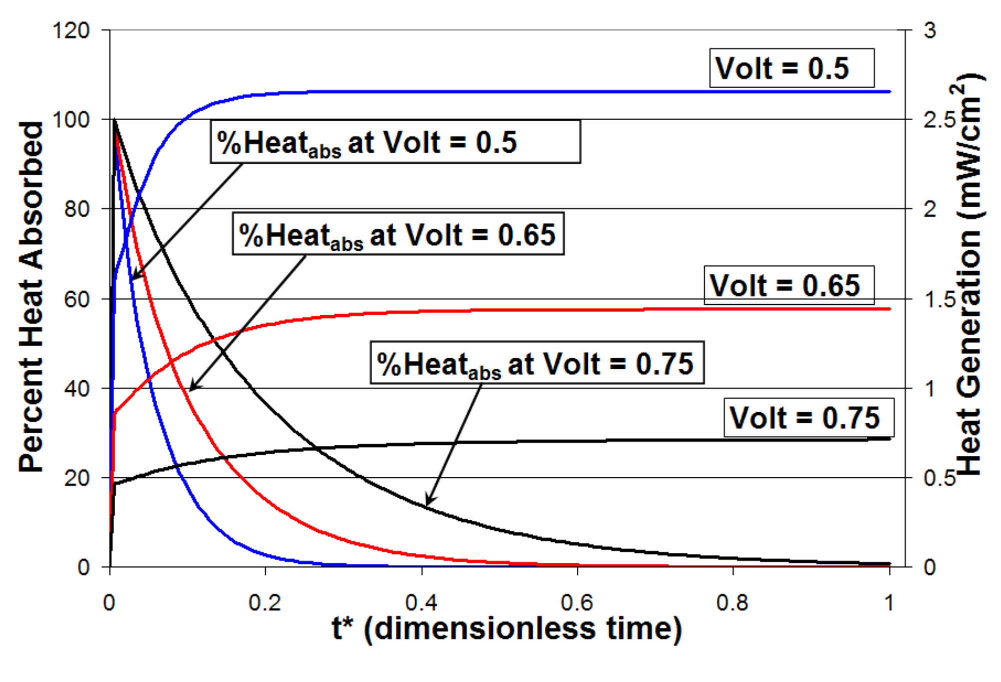

Figure 5.4. Heat generated by the cell and the percent of the heat retained by the cell for each scenario of the electrochemical light off simulations.

As expected, the cell power shown in Figure 5.5 is greater at lower cell potentials (i.e., higher current densities supersede the effect of lower cell potentials for typical operating regimes). However, the linearly increasing cell efficiency with cell potential, as quantified in Table 5.3, shows that there may exist an optimum condition for fuel efficient, yet rapid, SOFC heat-up.

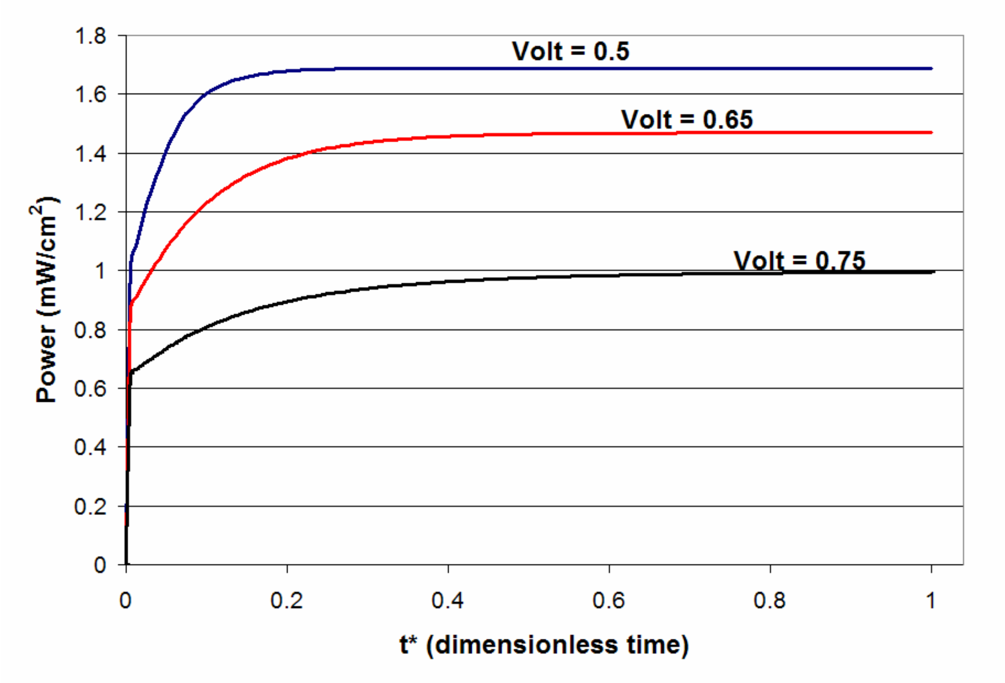

Figure 5.5. Power production for each electrochemical light off simulation.

Table 5.3. Final steady state cell efficiencies.

Cell Potential (V)	Efficiency (%)
0.50	34.1
0.65	44.4
0.75	51.2

Although the cell potential is the more natural spatial boundary condition, power electronics design preeminently considers current density as the dynamic control (i.e. a galvanostatic approach). Therefore, a galvanostatic approach was developed by modifying the potentiostatic approach to allow for current density to be the dynamic control. Four cases were run wherein current densities of 200, 300, 400, and 500 mA/cm^2 were the galvanostatic stimuli. These results were compared to potentiostatic simulations where the final steady-state current density matched that of each galvanostatic case. The temperature profiles of the two sets of simulations are compared in Figure 5.6.

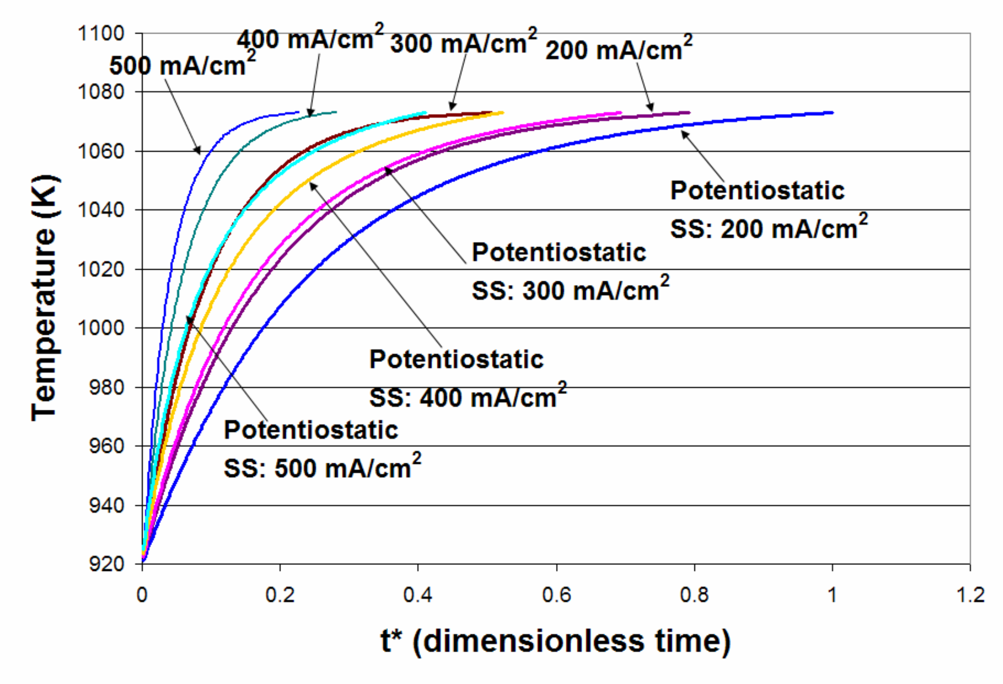

Figure 5.6. Temperature profiles for the galvanostatic and potentiostatic simulations of electrochemical light off.

There are two important observations depicted in Figure 5.6. The first observation is that cell heats up much more rapidly at higher current demands. Again, this is a result of the larger by-product heat generated at higher current demands. The second key result is that the galvanostatic approach heats the cell faster than that of the potentiostatic approach at each current density. The heat generation profiles shed light on the cause of faster heat up given a galvanostatic approach. Shown in Figure 5.7 are the heat generation profiles of both the galvanostatic and potentiostatic approach. In all of the galvanostatic cases, the heat generation is a maximum at the beginning of the simulation. This is because the ASR decreases with increasing temperature. Therefore, there is more by product heat generated (i.e. Joule heating) initially when ASR is at its maximum; hence, the heat generation is minimal at the operating temperature due the diminishing Joule heating effect for the galvanostatic cases. Given the potentiostatic cases, however, the heat generated is minimal at the beginning of the episode and reaches a maximum at the conclusion of the episode. This is due to the current density (and hence by-product heat generated) being minimal at the beginning of the electrochemical light off and increasing with temperature. Note that the maximum heat generated for the potentiostatic cases is equivalent to the minimum heat generated in the galvanostatic cases as can be seen in Figure 5.7; this is to be expected based upon convergences to final steady state conditions.

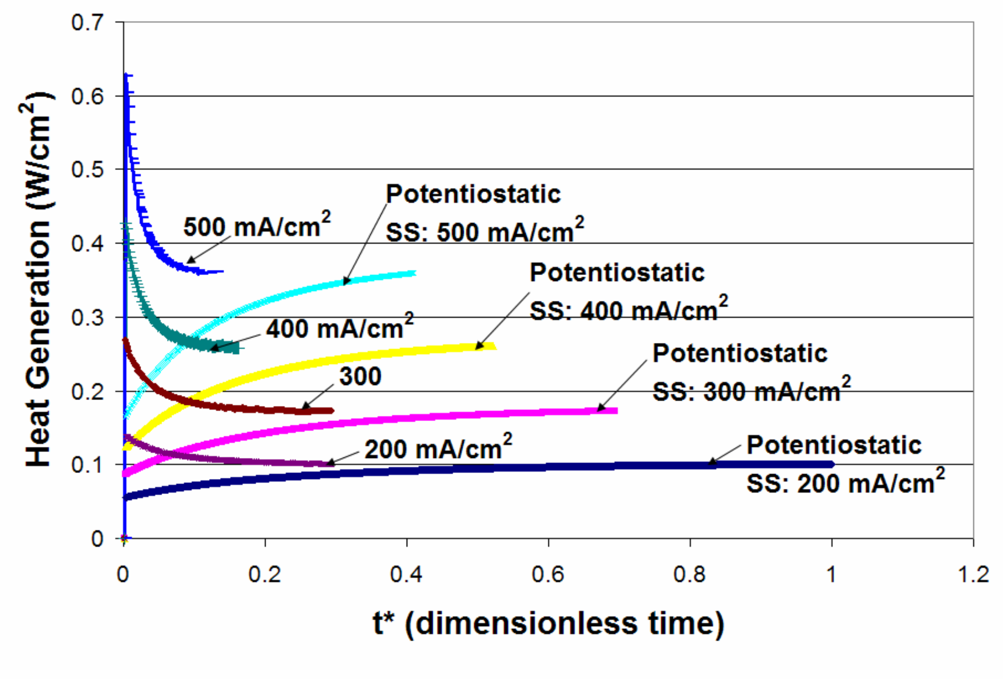

Figure 5.7. Heat generation profiles for the galvanostatic and potentiostatic simulations of electrochemical light off.

5.4 Conclusions of Electrochemical Light Off

It has been broached that cell potential is a viable dynamic control during cell heat up; hence, herein introducing the term "heating cell potential" is introduced. As an example, power electronics could be instituted to manage the heating cell potential, hence influence thermal transients, during the high temperature stages of thermal cycling. This result sheds light on the prospect of using electrochemical operating conditions to aid thermal management during transient heating and possibly mitigate thermal cycling issues. It was also shown that a galvanostatic approach heats the cell more rapidly than the potentiostatic case. In the next and final chapter, there will be a discussion of how the electrochemical light off simulation can be extended to simulate electrically-induced thermal (and corresponding polarization) hysteresis as well as other concluding remarks and future works items.

CHAPTER 6

CONCLUSIONS

6.1. Summary

The primary deliverable of the present thesis is an enhanced performance model of a SOFC that describes the transient response thereof to bi-modal stimuli and electrically stimulated thermal transients that occur during transitional heating of the cell (i.e. electrochemical light off). Complementary modeling efforts were completed in the thesis to further detail the necessity of transient anodic mass transfer model within electrical transient modeling. The enhanced electrical transient model developed in the thesis facilitated the simulation of downstream electrolysis, inclusive of the production of an operating map to predict the occurrence and location of electrolysis. Another key product of the thesis is the lumped capacitance electrochemical light off model which will be a forerunner for a future higher fidelity spatial-temporal thermal transient model.

6.2 Conclusions of Electrical Transient Modeling

A methodology has been developed to simulate the electrical transient responses to bi-modal stimuli (i.e. simultaneous changes in reactants supply rates and load demand). This is an enhancement beyond prevalent cell-/stack- level models in that there is an allowance for unslaved stack response to changes in load; such that reactant supply rates may also be transient. The “packet” and rediscretization methodologies were key developments to facilitate the modeling of bi-modal stimuli. It has been quantified how increasing fuel ramp (FRT) results in a more pronounced overshoot and undershoot in the fuel utilization and voltage profiles, respectively. The overshoot trend observed in the fuel utilization profile is due to the step increase in current demand combined with the delay in proportionate reactants supply. The increase in current coupled with a delay in reactant supply rate increase causes a resultant increase in reactant consumption via Faraday's law, thereby increasing the fuel utilization. Correspondingly, the local Nernst potential decreases and the concentration polarizations increases thereby stimulating the undershoot trend in the cell potential profile. Additionally, it was observed that the undershoot trend observed in the cell potential profile was less than 10%. Furthermore, if reactant supply rates are proportionally changed within one second, then the undershoot trend will decrease to 5%.

Although the modeling approach was instrumental, the code can be further developed in terms of validation, improved user interface, portability into other platforms, and improved computational efficiency. Extended parametric studies will ensue with the computational tools developed to further verify the code and explore the dynamic response of SOFCs.

6.3 Complementary Modeling Conclusions

6.3.1 Time Constant Analysis

The comparison of electrical and anodic mass transfer time constants was motivated by the need to ascertain the significance of anodic mass transfer transients relative to electrical (overarching) transients. A time constant ratio of ten is presumed sufficient to approximate quasi-steady state anodic mass transfer. In light of the results of Chapter 4, wherein some ratios are significantly less than ten, it has been concluded that anodic mass transfer transients are generally significant relative to electrical transients in numerous cases.

In addition to concluding that anodic mass transfer transients are generally significant relative to electrical transients, it was shown that initial current density, percent change in current, ASR, and anode thickness impact the electrical time constant. The complex trends observed in the electrical time constant profile is not completely understood. Therefore, extended investigation of the impact of fuel flow rate, fuel stream composition, and change in current on the electrical time constant to determine the root cause of the observed behavior is warranted. Lastly, both extreme FRT cases (i.e., FRT=0 and FRT $\rightarrow\infty$) produced identical time constant ratio mappings due to the fixed fuel supply rate condition (after t=0+) in both scenarios and hence the same relative fuel stream effects being replicated.

Since anodic mass transfer transients have been shown to be significant during electrical transients, there is then a need to develop transient anodic mass transfer models. Given the Lagrangian approach taken in the electrical transient model, an amenable modeling methodology may be to use a quasi-lumped capacitance anodic mass transfer modeling approach for each computational slice. More specifically, each slice is presumed to have a limited variation in composition; i.e., the transverse partial pressures of each constituent within the slice is presumed discretized over three distinct values: the partial pressure at the gas interface of the slice, approximated to be equal to the bulk stream value at the slice; a bulk average pressure that's the partial pressure over the vast height of the slice; and an electrolyte interface value as was detailed in Chapter 4.

6.3.2 Electrolysis Modeling

The electrolysis modeling of Chapter 4 created a map showing which operational conditions lead to down stream electrolysis. Such a mapping was developed due to the potential cell performance and reliability issues that given electrolytic operation of portions of the cell. It has been shown that fuel utilization and the magnitude of the decrease in current demand largely determine where electrolysis will occur downstream (i.e., the point of zero current where cell potential equals Nernst potential). A key observation is that at higher fuel utilizations there is a lower threshold for electrolysis to occur due to the significant decrease in axial Nernst potentials.

When electrolysis occurs during operation, the cell equilibrates thereby returning to normal operation. The current modeling approach only simulates when electrolysis will occur. Therefore, there is a need to model this equilibration process. The current electrical transient model can be modified to allow for negative currents in order to facilitate modeling of equilibration of the cell as was detailed by Gemmen and Johnson [31]. The electrical transient algorithm would have to be modified, but this work would offer a great feature to the current set of software developments.

6.4 Conclusions Electrochemical Light Off Simulations

It has been shown that cell potential is a viable dynamic control during cell heat up, thereby introducing the term "heating cell potential." As an example, power electronics control schemes could be instituted to manage the heating cell potential during transitional heating or thermal cycling of the cell. It was also shown that a galvanostatic approach heats the cell more rapidly than the potentiostatic case. These results shed light on the prospect of using electrochemical operating conditions to aid thermal management during transient heating and possibly mitigate thermal cycling issues.

In addition to the electrochemical light off phenomenon, additional electrically stimulated thermal transients arise during operation due to the heating effects within the SOFC. The lumped capacitance model developed for the electrochemical light off studies may be extended to model the thermal transients induced by load cycling. A thermal non-equilibrium condition is induced when the cell responds to a change in current demand. When these singular current changes are cyclical, the cell experiences a thermal cycle which may lead to a thermal hysteresis effect. Recently, a thermal hysteresis effect in SOFC materials has been experimentally observed [34, 35]. By varying the current density ramp rate (CDRR or dj/dt), the thermal hysteresis effect shown in Figure 6.1 is impacted. This thermal hysteresis will lead to voltage hysteresis effects as depicted in Figure 6.2. As an extension of the lumped capacitance illustration of a thermal hysteresis effect, the thermal model may be refined for higher fidelity spatial-temporal resolution. These results and developments will aid the needed characterization to mitigate cell reliability issues caused by thermal stresses/shock.

Similar to the electrical transient response modeling, extended parametric studies will ensue with the computational tools developed to further validate the code and explore the thermal dynamic response of SOFCs. The code will be embellished to make it more computationally efficient, “user friendly,” and portable (as MATLAB module(s)) to relevant end users.

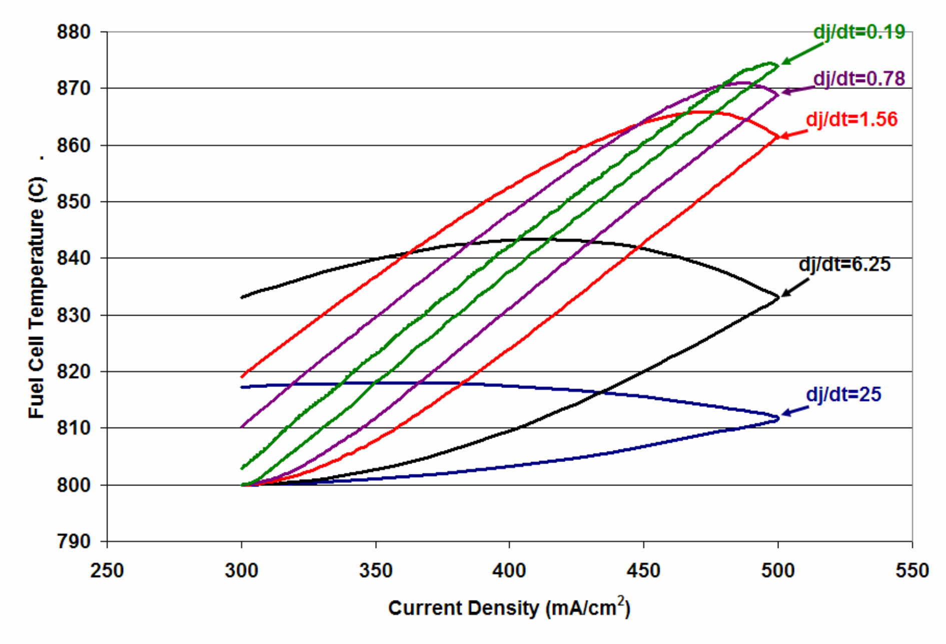

Figure 6.1. Graphic showing the thermal hysteresis effect caused by electrical load cycling between 300 mA/cm^2 to 500 mA/cm^2 which is impacted by the current density ramp rate (Note that CDRR or dj/dt has the units of mA/cm^2/min.)

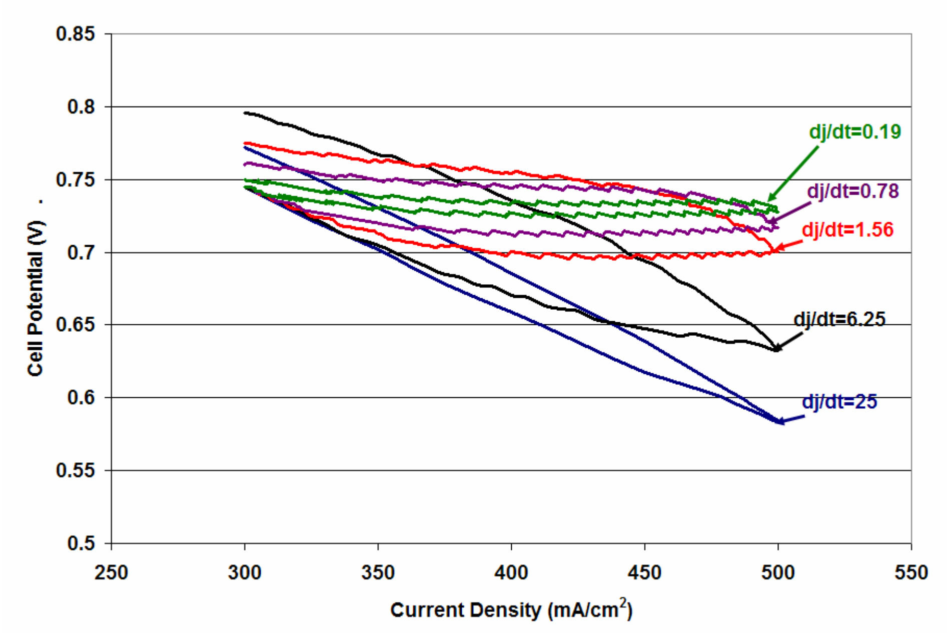

Figure 6.2. Graphic showing the voltage hysteresis effect caused by thermal hysteresis effect. (Note that CDRR or dj/dt has the units of mA/cm^2/min.)

REFERENCES

1. N.R.C., and N.A.C.E. (2004). "The Hydrogen Economy: Opportunities, Costs, Barriers, and R&D Needs." N. Research and Council, eds., National Academies Press: Washington, D.C.
2. Larminie, J., and Dicks, A. (2003). *Fuel cell Systems Explained*, A. Dicks, translator, J. Wiley, Chichester, West Sussex.
3. Haynes, C., and Rooker, W. (2002)"Thermal Management of Planar SOFCs via Design Optimation." *2002 Fuel Cell Seminar*, Palm Springs, California, November 18-21.
4. Haynes, C. (2002). "Simulating process settings for unslaved SOFC response to increases in load demand." *Journal of Power Sources*, 109(2), 365.
5. Sudaprasert, K., Travis, R. P., and Martinez-Botas, R. F. (2005). "A computational fluid dynamics model of a solid oxide fuel cell." *Proceedings of the Institution of Mechanical Engineers, Part A (Journal of Power and Energy)*, 219(A3), 159.
6. Larrain, D., Van Herle, J., Marechal, F., and Favrat, D. (2004). "Generalized model of planar SOFC repeat element for design optimization." 131, 304.
7. Li, P.-W., Schaefer, L., and Chyu, M. K. (2004). "A numerical model coupling the heat and gas species' transport processes in a tubular SOFC." *Journal of Heat Transfer*, 126(2), 219.
8. Aguiar, P., Adjiman, C. S., and Brandon, N. P. (2004). "Anode-supported intermediate temperature direct internal reforming solid oxide fuel cell. I: model-based steady-state performance." *Journal of Power Sources*, 138(1-2), 120.

9. Li, P.-W., and Suzuki, K. (2004). "Numerical Modeling and Performance Study of a Tubular SOFC." *Journal of the Electrochemical Society*, 151(4), 548-557.

10. Aguiar, P., Chadwick, D., and Kershenbaum, L. (2002). "Modeling of an indirect internal reforming solid oxide fuel cell." *Chemical Engineering Science*, 57(10), 1665.

11. Iwata, M., Hikosaka, T., Morita, M., Iwanari, T., Ito, K., Onda, K., Esaki, Y., Sakaki, Y., and Nagata, S. (2000). "Performance analysis of planar-type unit SOFC considering current and temperature distributions." *Solid State Ionics*, 132(3-4), 297.

12. Haynes, C., and Wepfer, W. J. (2000). "Design for power of a commercial grade tubular solid oxide fuel cell." *Energy Conversion and Management*, 41(11), 1123.

13. Ferguson, J. R., Fiard, J. M., and Herbin, R. (1996). "Three-dimensional numerical simulation for various geometries of solid oxide fuel cells." *Journal of Power Sources*, 58(2), 109.

14. Bessette, N. F., II, and Wepfer, W. J. (1995). "A mathematical model of a tubular solid oxide fuel cell." *Transactions of the ASME. Journal of Energy Resources Technology*, 117(1), 43.

15. Brandon, N. P., Aguiar, P., and Adjiman, C. S. (2005). "Anode-supported intermediate-temperature direct internal reforming solid oxide fuel cell." *Journal of Power Sources*, 147(1-2), 136.

16. Achenbach, E. (1994). "Three-dimensional and time-dependent simulation of a planar solid oxide fuel cell stack." 49, 333.

17. Achenbach, E. (1995). "Response of a solid oxide fuel cell to load change." *Journal of Power Sources*, 57(1-2), 105.

18. Sedghisigarchi, K., and Feliachi, A. (2004). "Dynamic and transient analysis of power distribution systems with fuel Cells-part I: fuel-cell dynamic model." *IEEE Transactions on Energy Conversion*, 19(2), 423.

19. Damm, D. L., and Fedorov, A. G. (2005)"Simplified thermal analysis of the SOFC transients during startup/shutdown." *Proceedings of the ASME Summer Heat Transfer Conference*, San Francisco, CA, United States, July 17-22.

20. Damm, D. L., and Fedorov, A. G. (2006). "Reduced-order transient thermal modeling for SOFC heating and cooling." *Journal of Power Sources*, 159(2), 956.

21. Petruzzi, L., Cocchi, S., and Fineschi, F. (2003). "A global thermo-electrochemical model for SOFC systems design and engineering." *Journal of Power Sources*, 118(1-2), 96.

22. Khaleel, M. A., Lin, Z., Singh, P., Surdoval, W., and Collin, D. (2004). "A finite element analysis modeling tool for solid oxide fuel cell development: coupled electrochemistry, thermal and flow analysis in MARC(R)." *Journal of Power Sources*, 130(1-2), 136.

23. (2004). *The Fuel Cell Handbook*, National Energy Technology Lab.

24. Bard, A. J., and Faulkner, L. R. (2001). *Electrochemical Methods: Fundamentals and Applications*, Wiley, New York.

25. Kim, J.-W., Virkar, A. V., Fung, K.-Z., Mehta, K., and Singhal, S. C. (1999). "Polarization effects in intermediate temperature, anode-supported solid oxide fuel cells." *Journal of the Electrochemical Society*, 146(1), 69.

26. Winnick, J. (1997). *Chemical Engineering Thermodyanics*, Wiley, New York.

27. Qi, Y., Huang, B., and Luo, J. (2006). "Dynamic modeling of a finite volume of solid oxide fuel cell: The effect of transport dynamics." *Chemical Engineering Science*, 61(18), 6057.

28. Gemmen, R. S., Famouri, P., and Johnson, C. (2003)"Assessing the Impact of Inverter Current-Ripple on SOFC performance." *Proceedings of the Fuel Cell Science, Engineering and Technology Conference*, Rochester, NY, April 21-23.

29. Gemmen, R. S., and Johnson, C. D. (2004)"Dynamics of solid oxide fuel cell operation." *Proceedings of the 2nd International Conference on Fuel Cell Science, Engineering and Technology*, Rochester, NY, June 14-17.

30. Gemmen, R. S., and Johnson, C. D. (2005). "Effect of load transients on SOFC operation--current reversal on loss of load." *Journal of Power Sources*, 144(1), 152.

31. Gemmen, R. S., and Johnson, C. D. (2006)"Thermal Gradient Induced Current Recirculation on Load Change in Solid Oxide Fuel Cells." *Proceedings of the Fuel Cell Science, Energy, and Technology Conference*, Irvine, CA, June 19-21.

32. Hawkes, G., O'Brien, J., Stoots, C., Herring, S., and Shahnam, M. (2005)"Thermal and electrochemical three dimensional CFD model of a planar solid oxide electrolysis cell." *Proceedings of the ASME Summer Heat Transfer Conference*, San Francisco, CA, United States, July 17-22.

33. Incropera, F. P., and DeWitt, D. P. (2002). *Fundamentals of Heat and Mass Transfer*, John Wiley and Sons, New York.

34. Park, C. Y., Azzarello, F. V., and Jacobson, A. J. (2006). "The oxygen non-stoichiometry and electrical conductivity of La(0.7)Sr(0.3)Cu(0.2)Fe(0.8)O(3-delta)." *Journal of Materials Chemistry*, 16(36), 3624.

35. Hashimoto, S., Kammer, K., Larsen, P. H., Poulsen, F. W., and Mogensen, M. (2005). "A study of Pr(0.7)Sr(0.3)Fe(1-x)Ni(x)O(3-delta) as a cathode material for SOFCs with intermediate operating temperature." *Solid State Ionics*, 176(11-12), 1013.

APPENDIX

VOLUMETRIC HEAT CAPACITANCE CALCULATION

A mass weighted approach was used to calculate the cell property data. The following four sets of equations and calculations were used to compute the unit cell heat capacitance and volumetric heat capacitance.

Mass (kg) Calculation: (A.1)

$$m_{anode} = \rho_{anode} t_{anode} L \cdot w_{cell} = 4200 \frac{kg}{m^3} \cdot 5x10^{-4}\, m \cdot 0.1m \cdot 5x10^{-3}\, m = 1.005x10^{-3}\, kg$$

$$m_{cathode} = \rho_{cathode} t_{cathode} L \cdot w_{cell} = 3300 \frac{kg}{m^3} \cdot 7.5x10^{-5}\, m \cdot 0.1m \cdot 5x10^{-3}\, m = 1.238x10^{-4}\, kg$$

$$m_{electrolyte} = \rho_{electrolytee} t_{electrolyte} L \cdot w_{cell} = 5100 \frac{kg}{m^3} \cdot 1.5x10^{-5}\, m \cdot 0.1m \cdot 5x10^{-3}\, m = 3.83x10^{-5}\, kg$$

$$m_{\mathrm{int}\,erconnect} = \rho_{\mathrm{int}\,erconnect} \left(t_{\mathrm{int}\,erconnect} \cdot w_{cell} - w_{channel} \cdot h_{channel}\right) L$$

$$m_{\mathrm{int}\,erconnect} = 8055 \frac{kg}{m^3} \cdot \left(5x10^{-3}\, m \cdot 5x10^{-3}\, m - 2.5x10^{-3} \cdot 2.5x10^{-3}\right) 0.1m = 1.510x10^{-2}\, kg$$

$$m_{cell} = m_{anode} + m_{cathode} + m_{electrolyte} + 2 \cdot m_{\mathrm{int}\,erconnect}$$

$$m_{cell} = 1.005x10^{-3}\, kg + 1.238x10^{-4}\, kg + 3.83x10^{-5}\, kg + 2 \cdot 1.510x10^{-2}\, kg$$

$$m_{cell} = 3.14x10^{-2}\, kg$$

Specific Heat (J/kg-K) Calculation: (A.2)

$$c_{cell} = \frac{m_{anode} c_{anode}}{m_{cell}} + \frac{m_{cathode} c_{cathode}}{m_{cell}} + \frac{m_{electrolyte} c_{electrolyte}}{m_{cell}} + \frac{2 \cdot m_{\mathrm{int}\,erconnect} c_{\mathrm{int}\,erconnect}}{m_{cell}}$$

Heat Capacitance (J/K): (A.3)

$$C_{cell} = m_{cell}\cdot c_{cell} = m_{cell}\left(\frac{m_{anode}c_{anode}}{m_{cell}} + \frac{m_{cathode}c_{cathode}}{m_{cell}} + \frac{m_{electrolyte}c_{electrolyte}}{m_{cell}} + \frac{2\cdot m_{\mathrm{int}\,erconnect}c_{\mathrm{int}\,erconnect}}{m_{cell}}\right)$$

$$C_{cell} = m_{anode}c_{anode} + m_{cathode}c_{cathode} + m_{electrolyte}c_{electrolyte} + 2\cdot m_{\mathrm{int}\,erconnect}c_{\mathrm{int}\,erconnect}$$

$$C_{cell} = 1.005x10^{-3}\,kg\cdot 640\frac{J}{kg-K} + 1.2375x10^{-4}\,kg\cdot 570\frac{J}{kg-K}$$

$$3.825x10^{-5}\,kg\cdot 600\frac{J}{kg-K} + 2\cdot 1.51x10^{-2}\,kg\cdot 623\frac{J}{kg-K}\ \backslash$$

$$C_{cell} = 19.55\frac{J}{K}$$

Volumetric Heat Capacitance: (A.4)

$$C_{cell,volumetric} = \frac{C_{cell}}{V}$$

$$V = L\cdot w_{cell}\cdot\left(t_{anode} + t_{cathode} + t_{electrolyte} + 2\cdot t_{\mathrm{int}\,erconnect}\right) - V_{flow\ channels}$$

$$V_{flow\ \ channels} = 2\cdot w_{channel}\cdot h_{channel}\cdot L$$

$$V_{flow\ \ channels} = 2\cdot 2.5x10^{-3}\,m\cdot 2.5x10^{-3}\,m\cdot 0.1m = 1.25x10^{-6}\,m^3$$

$$V = 0.1m\cdot 5x10^{-3}\,m\cdot\left(5x10^{-4}\,m + 7.5x10^{-5}\,m + 1.5x10^{-4}\,m + 2\cdot 5x10^{-3}\,m\right) - 1.25x10^{-6}\,m^3$$

$$V = 4.11x10^{-6}\,m^3$$

$$C_{cell,volumetric} = \frac{19.55}{4.11x10^{-6}}\frac{J}{m^3K} = 4.76\frac{MJ}{m^3K} = 4.76\frac{J}{cm^3K}$$

Note: The specific heat of the stainless-steel interconnects is temperature dependent and in the above calculations a temperature of 1073 K was used to obtain the stated values.